Title: Glial *betaPix* is essential for blood vessel integrity in the zebrafish brain

ShihChing Chiu[1], Qinchao Zhou[1], Chenglu Xiao[2], Linlu Bai[1], Xiaojun Zhu[1,*], Wanqiu Ding[1,*], and Jing-Wei Xiong[1,2,*,#]

[1]Beijing Key Laboratory of Cardiometabolic Molecular Medicine, Institute of Molecular Medicine, and College of Future Technology, Peking University, Beijing 100871, China; [2]School of Basic Medical Sciences, The Second Affiliated Hospital, Institute of Biomedical Innovation, The MOE Basic Research and Innovation Center for the Targeted Therapeutics of Solid Tumors, Jiangxi Medical College, Nanchang University, Nanchang 330031, China

*Corresponding authors: WD (dingwq@pku.edu.cn), XZ (zhuxiaojun@pku.edu.cn), and JWX (jingwei_xiong@pku.edu.cn)

#Lead Contact: Jing-Wei Xiong, Ph.D. (jingwei_xiong@pku.edu.cn)

Abstract

The formation of blood-brain barrier and vascular integrity depends on the coordinative development of different cell types in the brain. Previous studies have shown that zebrafish *bubblehead* (*bbh*) mutant, which has mutation in the *betaPix* locus, develops spontaneous intracerebral hemorrhage during early development. However, it remains unclear in which brain cells *betaPix* may function. Here, we established a highly efficient conditional knockout method in zebrafish by using homology-directed repair (HDR)-mediated knockin and knockout technology, and generated *betaPix* conditional trap (*betaPix*^{ct}) allele in zebrafish. We found that *betaPix* in glia, but neither neurons, endothelial cells, nor pericytes, was critical for glial and vascular development and integrity, thus contributing to the formation of blood-brain barrier. Single-cell transcriptome profiling revealed that microtubule aggregation signaling stathmins and pro-angiogenic transcription factors *Zfhx3/4* were down-regulated in glial and neuronal progenitors, and further genetic analysis suggested that betaPix acted upstream on the PAK1-Stathmin and Zfhx3/4-Vegfaa signaling to regulate glia migration and vascular integrity. Therefore, this work reveals that glial *betaPix* plays an important role in brain vascular integrity in zebrafish embryos and possibly human cells.

Keywords: *betaPix*; hemorrhage; glial migration; knock-in; stathmin

Introduction

Intracerebral hemorrhage (ICH) is a life-threatening stroke type with the worst prognosis and few proven clinical treatments. Most patients who survive intracerebral hemorrhage end up with disabilities and are at risk for recurrency, cognitive decline, and systemic vascular issues, making this condition particularly significant among neurological disorders [1,2]. Several rodent models have been used for modeling ICH, including autologous blood injection, collagenase injection, thrombin injection, and micro-balloon inflation techniques [3]. Zebrafish (Danio rerio) exhibit a closed circulatory system and regulatory pathways that are highly conserved among vertebrates [4] with relatively cheap and easy to maintain disease models. Over the past decades, varieties of zebrafish mutants that spontaneously developed brain hemorrhage have been generated in mutagenesis screens, such as *redhead* [5], *reddish* [6,7] and *bubblehead* (*bbh*) [8,9]. Elucidating mutated gene function in these zebrafish models enables us to gain insights into the genetic basis and pathophysiological mechanisms of ICH development. The *bbh* mutant was identified independently in two large-scale ethylnitrosourea-induced mutagenesis screens [8,9] and positional cloning revealed that p21-activated kinase (Pak)-interacting exchange factor beta (*betaPix*) gene was mutated in *bbh* mutants [10]. *betaPix* contains SH3 domain that binds group I PAKs, and Dbl homology (DH) and pleckstrin homology (PH) domains that function as a RhoGEF to interact with Rac/Cdc42 small GTPases [11], thus participating in multiple cellular pathways to regulate cell polarity, adhesion and migration [12].

Various studies have reported that brain vessels are highly supported by neurons and glial cells during development and regeneration [13,14]. Glial-specific *betaPix* have been proposed to interact with *αvβ8* integrin and the Band 4.1s in glia, which link to multiple intracellular signaling effectors such as *Wnt7a* and *Wnt7b* [15], but this hypothesis was not experimentally addressed [16]. To this end, *betaPix* has been shown to interact with *αvβ8* integrins and mediate focal adhesion formation and thus modulate cerebral vascular stability in *bbh* zebrafish mutant [17]. Integrins are the main molecular link between cells and the extracellular matrix (ECM) which serve as scaffolds in the perivascular space. Based on a chemical suppressor screening of *bbh* hemorrhages, we have previously reported that a small molecule called miconazole downregulated the pErk-matrix metalloproteinase 9 (Mmp9) signaling to reduce ECM degradation, thus improving vascular integrity [18]. However, how *betaPix* cell-type specifically contributes to vascular integrity and maturation remains unclear. Here, we generated *betaPix* conditional trap (*betaPix*^{ct}) alleles by using a CRISPR/HDR-based Zwitch method, and found that betaPix acted mainly in glia to regulate glial and vascular integrity *via* Stathmin and Zfhx3/4 signaling. Therefore, this work provides the first experimental evidence that betaPix acts in glia for vascular integrity development, and its functional conservation between zebrafish and human cells may further guide us to decipher the genetic basis of ICH in the future.

87 **Results**

88 **Generating *betaPix* conditional trap (*betaPix^{ct}*) allele by an HDR-mediated**

89 **knockin and knockout method**

90 To study *betaPix* function in cell-specific manner, we utilized a donor vector with an

91 invertible gene trap cassette *via* HDR (Zwitch) [19-21] for generating *betaPix* conditional

92 trap (*betaPix^{ct}*) alleles. Zwitch consists of a splice acceptor conjugated to a red

93 fluorescent protein *via* a 2A self-cleaving peptide, flanked by two LoxP sites and two

94 Lox 5171 sites in reciprocal orientations. Outside this conditional trap cassette, we

95 included a lens-specific enhanced green fluorescence protein *α*-crystallin:EGFP for

96 screening knockout founders, as well as inserted both left and right arms for targeting

97 homologous sequences on the genome. We modified the Zwitch vector by adding a

98 glycine-serine-glycine (GSG) spacer in front of the 2A peptide to enhance cleavage

99 efficiency, and adding universal guide RNA (UgRNA)[22] target sequences outside the

100 left and right homologous arms for linearizing donor vector (Figures 1A and S1A). We

101 chose CRISPR/Cas9 system to generate double-strand breaks (DSBs) on intron 5 of the

102 *betaPix* locus, and chose the most efficient guide RNAs based on their efficiency to

103 induce CRISPR indels. We used either long arms such as ~1000 bp or short arms such

104 as 24 bp that located upstream and downstream the guide RNA sites. We then co-

105 injected the donor vectors with targeting guide RNA, universal guide RNA, and Cas9

106 mRNA into one-cell-stage embryos. At 4 days post-fertilization (dpf), we selected *α*-

107 crystallin-EGFP-positive embryos (F_0) for raising to adulthood, and pre-selected F_0

108 founders by examining inheritable EGFP reporter expression of F_1 embryos. To confirm

109 the correct homologous recombination in the *betaPix* locus, we identified potential
110 founders by genomic PCR to examine Zwitch insertion in the *betaPix* locus. Precise
111 knock-in genotypes were further verified using Sanger sequencing (Figures 1B, 1C,
112 S1B). Among 184 adult F_0 founders with α-crystallin-EGFP expression, we found 84
113 founders had EGFP-positive F_1 embryos, and 7 founders had expected PCR fragments
114 around both 5' and 3' arms, which two founders had correct insertions in the *betaPix*
115 locus by Sanger sequencing (Figure S1C), thus achieving ~1% efficiency on generating
116 conditional alleles. Briefly, we established an efficient method for generating
117 conditional knockin/knockout mutants in general, and generated a conditional gene trap
118 line Ki(*betaPix*:Zwitch) in the *betaPix* locus in particular, which is referred to as
119 $betaPix^{ct}$ hereafter.
120
121 A previous work has shown *bubblehead* (bbh^{m292}) mutant with a hypomorphic mutation
122 in *betaPix*, and bbh^{fn40a} mutant with reduced *betaPix* transcripts without finding
123 mutations in the coding region and the splicing sites [10]. bbh^{fn40a} mutants developed
124 cerebral hemorrhages phenotype between 36 to 52 hpf (Figure S1D and S1E). To
125 characterize the $betaPix^{ct}$ allele, we injected one-cell-stage $betaPix^{ct/ct}$ embryos with
126 *Cre* mRNA to induce global inversion of Zwitch and deletion of *betaPix*. As expected,
127 we found Cre-induced precise inversion in $betaPix^{m/m}$ as confirmed by Sanger
128 sequencing (Figure 1C) and severe brain hemorrhages developed in the time window
129 similar to bbh^{fn40a} mutants (Figures 1D and 1E). Consistently, qPCR analysis showed
130 that *betaPix* decreased and *RFP* increased in heterozygous $betaPix^{m/+}$ and homozygous

131 *betaPix*$^{m/m}$ mutants compared with *betaPix*$^{ct/ct}$ wild-type siblings, while *alphaPix*
132 expression was not affected (Figure 1F). Of note, *TagRFP* expression in *betaPix*$^{m/+}$
133 (after Cre-mediated recombination in *betaPix*$^{ct/+}$ embryos) reflected endogenous
134 *betaPix* expression in the boundary of midbrains and hindbrains as well as the
135 hindbrains (Figure S1F and S1G). Together, these results suggest that the conditional
136 trap *betaPix*$^{ct/ct}$ zebrafish is functional for visualizing endogenous *betaPix* expression
137 (knockin) and loss-of-function study (conditional knockout).
138

139 **_betaPix_$^{m/m}$ mutant has brain hemorrhages, central arteries defects and abnormal**
140 **glial structure that is partially rescued by Pak1 inhibitor IPA3 treatment**

141 The main phenotypes in *bbh* mutants consist of brain hemorrhage and hydrocephalus
142 as early as 36 hpf, as well as poor endothelial–mesenchymal contacts and defective
143 central arteries (CtAs) sprouting in the hindbrain [10,17]. To demonstrate the practicability
144 of *betaPix* conditional trap lines, we assessed vasculature and glia in the hindbrain by
145 using light sheet fluorescence microscopy. Global *betaPix* inactivation in *betaPix*$^{m/m}$
146 mutants resulted in severe cerebral hemorrhages and defective angiogenesis in
147 hindbrain central arteries (Figures 1D, 1E, S2A and S2B), which is consistent with
148 previous studies [10,18].
149

150 It has been suggested that endothelial *betaPix* might not contribute to the occurrence of
151 brain hemorrhage [10]. During brain development, neurons and glia are important
152 perivascular cells and they orchestrate with endothelial cells in a temporal and spatial

153 pattern. Thus, we studied hindbrain radial glia development and found that radial glial
154 structure had disoriented arrangement and shorten process length in *betaPix*$^{m/m}$ embryos
155 compared to siblings (Figures 2A, 2B and S2C). As a result, neuronal and glial
156 precursors marker *nestin* increased while differentiated neuronal marker *pax2a*
157 decreased in *betaPix*$^{m/m}$ embryos, suggesting delayed neuronal development and
158 differentiation after *betaPix* inactivation (Figure 2C). By using global *betaPix* knockout
159 with multiple guide-RNA simultaneously [23], we found that CRISPR-induced *betaPix*
160 mutant F_0 embryos had almost identical phenotypes to those in *betaPix*^{fn40a} mutants
161 (Figure S3A-S3B), such as cerebral hemorrhages, central arteries defects, and abnormal
162 hindbrain glia and neuronal precursor development (Figures S3C to S3G), further
163 confirming the loss-of-function phenotypes in *betaPix*$^{m/m}$ mutants.
164
165 Zebrafish central arteries vascularization in the hindbrains starts at 29 hpf. Tip cells
166 start to form in the dorsal side of the primordial hindbrain channels (PHBC), sprout and
167 migrate into the hindbrain tissue, moving towards the center around 36 hpf to establish
168 connections with the basilar artery. A characteristic arch architecture forms at 48 hpf as
169 boundaries dividing the hindbrain into rhombomeres[24]. In *betaPix* knockouts, CtA
170 sproutings were restricted to the bottom of glial processes, thus not being able to
171 migrate upwards to form an arched structure (Figure 2D). The transcription factor SRY
172 box-2 (Sox2) is another marker gene for neuron and glial precursors. *Sox2*-positive
173 precursor cells tightly wrapped around the central artery in control siblings, but Sox2
174 precursor cells had loose contacts with the central arteries, with larger perivascular

175 distances in *betaPix* mutants (Figure 2E). These results implicate the impaired
176 interactions between endothelial cells and neuronal/glial cells during development after
177 *betaPix* deletion.
178
179 p21-activated kinase (Pak) is a binding partner for *betaPix*. *Pak2a* has been shown
180 mediating downstream signaling in bbh^{m292} mutants. Group I PAK allosteric
181 inhibitor IPA-3 covalently modifies and stabilizes the autoinhibitory N-terminal
182 region of PAK1, PAK2 and PAK3 [25]. As expected, IPA-3 treatment significantly
183 decreased incidence and intensity of cerebral hemorrhages in $betaPix^{m/m}$ mutant
184 embryos (Figure 2F and 2G), while IPA-3 treatment had no effect on hematopoiesis in
185 $betaPix^{ct/ct}$ control siblings. In addition, central arterial defects were partially rescued
186 in $betaPix^{m/m}$ mutant embryos after IPA-3 treatment, showing increased endothelial
187 protruding into the hindbrain and more arch structure formation (Figure 2H and 2I).
188 IPA-3 treatment also decreased abnormal glial process arrangements, which the
189 lengths of glial processes statistically reached the levels of the control siblings (Figure
190 2J). Thus, these data suggest that the betaPix-Pak1/2 signaling regulates brain
191 vascular integrity during development.
192
193 **Glial-specific *betaPix* knockouts recapture its global knockout phenotypes**
194 To investigate *betaPix* function in different types of perivascular cells, we generated
195 glial- or neuronal-specific transgenic lines using either glial fibrillary acidic protein
196 (*gfap*) [26] or *huC* [27] promoters to drive *EGFP-Cre* fusion gene expression under

197 *betaPix*$^{ct/ct}$ background, respectively (Figure S4A). EGFP signals reported *Cre*
198 expression while RFP signals efficiently reported Cre-induced gene trap cassette
199 inversion and disruption of *betaPix* expressions (Figure S4B to S4F). Interestingly,
200 glial-specific *betaPix* knockouts developed severe cerebral hemorrhages and abnormal
201 central arteries vascularization, which were partially rescued by IPA-3 treatment
202 (Figure 3A to 3C), highlighting betaPix function in glia *via* Pak1/2 signaling. On the
203 other hand, neither vascular-, neuronal-, nor mural-specific deletion of *betaPix* had
204 evident *betaPix* mutant phenotypes (Figure S5A to S5D). These results suggest that
205 glial *betaPix* plays crucial roles in zebrafish embryonic vascular integrity and glial
206 development *via* regulating *Pak* activities.
207

208 **Single-cell transcriptome profiling reveals that stathmins in *gfap*-positive**
209 **progenitors were affected in *betaPix* knockouts**

210 To investigate the interplays between glial and hemorrhagic pathology caused by
211 *betaPix* loss-of-function, we profiled the cranial tissues of CRISPR-edited zebrafish at
212 1 and 2 dpf using the 10X Chromium single-cell RNA sequencing (scRNA-seq)
213 platform (Figure 4A). Multi-guide targeting was able to generate almost 100% F_0 null
214 mutants, allowing us to select mutant embryos before brain hemorrhages from 36 hpf.
215 Low-quality cells were excluded based on the numbers of genes detected and
216 percentages of reads mapped to mitochondrial genes per sample. A total of 38,670 cells
217 passed quality control and were used for subsequent analyses. Uniform manifold
218 approximation and projection (UMAP) identified 71 cell clusters, which represented 24

219 zebrafish cranial cell types based on known marker gene expression profiles (Figure 4B
220 and S6A). Enriched gene markers were compared with previously annotated gene
221 markers in the ZFIN database and literatures[28,29]. By comparing the proportion of cells
222 in each sample, we found that most neuronal clusters had increased trends, while the
223 numbers of progenitors, endothelial cells, erythrocytes, neural crests, muscles,
224 cartilages, retinas (photoreceptor precursor cells), olfactory bulbs, or epidermis and
225 pharyneal arches were reduced in *betaPix* knockout heads at 2 dpf (Figure 4C and S6B).
226 This is consistent with the open public databases of single-cell transcriptome atlas
227 where *betaPix* weakly expressed in a broad range of cells including glia, neurons and
228 neuronal precursors, retinas, endothelial cells, pharynx, exocrine pancreas, olfactory
229 cells and heart cells [30]. Given that *betaPix* is critical in glia during brain vascular
230 integrity development (Figures 3 and S5), we examined the *gfap* expression among
231 each cluster, and found relatively high *gfap* expression in clusters including progenitors,
232 hindbrain, ventral diencephalon, ventral midbrain and floor plate (Figure S6A, arrow
233 indicates). We next focused on the progenitor cluster, as of its enriched *gfap* expression
234 and relatively more decreased cell numbers in *betaPix* mutants. Furthermore, this
235 progenitor cluster exhibited high-level expression of cell proliferation and cell cycle
236 related genes (*mki67*, *pcna*, *ccnd1*, *rrm1* and *rrm2*) as well as key glial-associated genes
237 (*gfap*, *fabp7a*, *her4*.1, *cx43*, *id1*, *fgfbp3*, *atp1a1b* and *mdka*) (Table S1). From
238 differentially expressed genes (DEGs) in this progenitor cluster between controls and
239 *betaPix* knockouts at 2 dpf, enriched gene ontology (GO) terms revealed three major
240 categories: epigenetic remodeling including chromatin silencing, negative regulation of

241 transcription, chromatin packaging and nucleosome positioning; microtubule
242 organizations including microtubule depolymerization, regulation of microtubule
243 polymerization and microtubule cytoskeleton organization; and neurotransmitter
244 secretion/transportation (Figure 4D). Of these signaling genes, we were particularly
245 interested in microtubule genes for further studies.
246

247 **Stathmin acts downstream of *betaPix* in glial migration *via* regulating tubulin**
248 **polymerization**

249 Microtubules are essential cytoskeletal elements composed of α/β-tubulin heterodimers.
250 The regulation of microtubule polymerization affects important cellular functions such
251 as mitosis, motor transport, and migration [31]. Based on the above scRNA-seq data
252 (Figures 4E and S6C), we then examined if microtubule polymerization genes
253 stathmins were affected in *betaPix* mutants. We found that stathmin1a (*stmn1a*),
254 stathmin1b (*stmn1b*), and stathmin4l (*stmn4l*) were relatively abundant in both the
255 whole brain and the progenitor cluster, and decreased specifically at 2dpf in *betaPix*
256 knockout progenitor cells (Figure 4E). Subsequent qRT-PCR revealed that these
257 stathmins expression decreased in both global *betaPix* knockouts (*betaPix*$^{m/m}$) and glial-
258 specific betaPix knockout glia (*gfap*:EGFP-Cre;*betaPix*$^{ct/ct}$) (Figure 4F and 4G), which
259 was further verified by RNA *in situ* hybridization analysis (Figure 4H). We next
260 investigated whether *Stathmins* act downstream to *betaPix* signaling on regulating
261 vascular integrity development. To this end, we found that *Pak1/2* inhibition enabled to
262 rescue down-regulated expressions of *stmn1a*, *1b* and *4l* in either global or glial-specific

263 *betaPix* knockout zebrafish (Figures 5A, 5B and S7A), supporting previous findings
264 that *stathmin-1* acts downstream to *betaPix-Pak* signaling in neurite outgrowth in
265 mice[32].
266
267 To test whether *Stathmin* family genes are important for vascular stability, we utilized
268 CRISPR-induced F_0 knockout system simultaneously targeting the three stathmin genes.
269 While singular stathmin gene knockout led to no evident phenotypes (data not shown),
270 we found that simultaneously inactivating *stmn1a*, *stmn1b* and *stmn4l* caused brain
271 hemorrhages and hydrocephalus in the brain, similar to that from *betaPix*^{fn40a} *and*
272 *betaPix*$^{m/m}$ mutants (Figures 5C, 5D, S7B to S7E). By labeling both glia and vasculature
273 with Tg(*gfap*:GFP; *kdrl*:mCherrry) transgenic embryos, we found that triple stathmin
274 gene knockouts had impaired CtAs, abnormal glia and neuronal development in the
275 hindbrain region (Figure 5E, 5F, S7F to S7H). Furthermore, overexpressing *stmn1b* by
276 the *gfap* promoter partially rescued brain hemorrhages and delayed neuronal
277 development in *bbh*^{fn40a} mutants (Figures 5G, 5H, S7I and S7J), of which glial processes
278 elongation also improved, but CtAs defects failed to restore (Figures 5I, 5J and S7K).
279 Thus, these data support the critical role of stathmins in glia.
280
281 To examine the direct role of *betaPix-stathmin* in glia, we turned to use human
282 glioblastoma cell lines and manipulated the *betaPix* levels by siRNA knockdown or
283 transgenic overexpression. We found that *betaPix* knockdown attenuated glial
284 migration (Figures 5K, 5L, S7L to S7N), which is consistent with previous studies on

285 *betaPix* function in the endoderm [33], epithelial cells [34], neurons [35] and multiple
286 carcinoma cell lines including glioblastoma [36-38]. Either *betaPix* or *Stmn1*
287 overexpression led to a partial restoration of the impaired glial migration, suggesting
288 *Stathmins* as downstream effectors of *betaPix*. Furthermore, immunofluorescence
289 analysis revealed that *betaPix* knockdown led to abnormal accumulation of
290 microtubules at the cell periphery, whereas ectopic expression of *betaPix* and *Stathmin*
291 partially rescued these microtubule defects (Figures 5M and 5N). Together, these
292 results suggest that *betaPix* depletion disrupts microtubule dynamics and leads to
293 impaired glial development acting upstream to the *Pak-Stathmin* signaling,
294 subsequently disrupting vascular integrity and resulting in brain hemorrhages. While
295 the brain hemorrhages were only partially rescued and abnormal CtAs defects failed to
296 restore, indicating that additional pathways may act downstream of *betaPix*.
297
298 ***Zfhx3/4* acts downstream of *betaPix* in regulating vascular integrity development.**
299 Previous studies have identified multiple signaling pathways important for zebrafish
300 hindbrain angiogenic sprouting, such as VEGF, Notch, Wnt, Integrin β1,
301 angiopoietin/TIE, and insulin-like growth factor signaling [39-42]. To investigate whether
302 angiogenic signal is disrupted by *betaPix* depletion, we examined several angiogenic
303 gene expression pattern by performing RNA *in situ* hybridization of embryos at 36 hpf.
304 The expression level of *Vegfaa* in sprouting CtAs decreased in bbh^{fn40a} mutants (Figure
305 6A). Consistently, *betaPix* knockdown significantly reduced *VEGFA* expression in
306 cultured glial cells, which was rescued by ectopic expression of *betaPix* (Figure 6B;

307 right panel). To explore how *betaPix* regulate *Vegf* signaling in glia, we also found a
308 significant enrichment of epigenetic and transcriptional regulation in progenitor cluster
309 indicated by the GO analysis of single-cell sequencing data (Figure 4D). Among these
310 candidate genes, transcription factor Zinc Finger Homeobox 3 (ZFHX3) is known to
311 mediate hypoxia-induced angiogenesis in hepatocellular carcinoma *via* transcriptional
312 activation of VEGFA [43]. Furthermore, ZFHX3 has been associated with stroke in
313 multiple genome-wide association studies [44-46]. Interestingly, we found that
314 transcription factors *Zfhx3* and *Zfhx4* significantly downregulated after *betaPix*
315 inactivation in cultured glial cells (Figure 6B), CRISPR-induced *betaPix* mutants at 2
316 dpf (Figure S8A), and glia-specific *betaPix* mutants (Figure S8B), thus suggesting that
317 *betaPix* acts upstream to Zfhx3/4-VEGFA signaling in regulating angiogenesis.
318
319 To determine whether *Zfhx3/4* is critical for vascular integrity by interacting with
320 *betaPix* in zebrafish, we depleted *Zfhx3* and *Zfhx4* simultaneously *via* CRISPR-
321 mediated F_0 knockouts (Figure S8C to S8E). We found that *zfhx3/4* knockouts
322 decreased *Vegfaa* expression at sprouting CtAs at 36 hpf (Figure 6C). *Zfhx3/4*
323 knockouts at 48 hpf had under-developed CtAs and reduced penetration of endothelial
324 cells into the hindbrain (Figure 6F and 6G), developed cerebral hemorrhages during 36
325 to 52 hpf, which are comparable with *betaPix* mutant phenotypes (Figure 6D-6G).
326 Despite up-regulated expression level of *nestin*, glial arrangement and processes
327 elongation remained statistically unaffected after *Zfhx3/4* inactivation (Figures 6F, 6G
328 and S8F). We next investigated whether increasing expression level of *Vegfaa* in

329 *betaPix* mutants was able to rescue impaired vascular integrity. By using *Zfhx4* mRNA
330 microinjection into one-cell stage embryos in either *bbh*^{fn40a} mutants or CRISPR-
331 induced *betaPix* knockouts, we found that ectopic expression of *Zfhx4* increased *Vegfaa*
332 expression level (Figure 6L), thus leading to a drastic reduction of both percentages and
333 volumes of brain hemorrhage shown in these mutants (Figures 6H, 6I, S8G to S8I), as
334 well as improved CtAs and glial development (Figures 6J and 6K). In addition, scRNA-
335 seq data showed that CRISPR-induced *betaPix* knockouts had down-regulated
336 angiogenic gene expression in a cluster of endothelial cells (Figure 6M). Together, these
337 data support the critical role of *Zfhx3/4* in vascular integrity and glial development
338 probably acting upstream to VEGFA and downstream to betaPix.
339

340 **Discussion**

341 Conditional knockout technology in mice has been widely used to modify and
342 determine targeted gene function in a cell-specific manner. Spatio-temporal specific
343 modification is beneficial for studying embryonic lethality genes or investigating the
344 function of targeted genes in specific cell populations. Despite being broadly utilized
345 in mice, conditional knockouts in other animal models are limited due to technical
346 difficulties. To this end, multiple research groups have designed different strategies
347 for establishing floxed-mutant alleles, gene traps, and inducible Cas9 in zebrafish [47].
348 In particular, the Zwitch gene trap-based approach has been established successfully
349 in zebrafish, enabling to simultaneously produce knockin reporter driven by the
350 endogenous gene promoter and disrupting endogenous gene function [19-21]. We adapted

351 this strategy with the aid of CRISPR/Cas9 technology, and added a GSG spacer to
352 enhance cleavage efficiency and universal guide RNA target sites on both
353 homologous arms for producing linearized targeting vector. Moreover, we also found
354 that utilizing either short or long homologous arms enables to achieve precise targeted
355 integrations with this donor vector. Our short arms-based method can be broadly
356 adapted because of less restrictions on arm sequences and easily engineering the
357 donor vector. From the *betaPix* locus and other five unpublished loci that we already
358 generated Zwitch alleles with ~1% correct insertions based on homologous
359 recombination, we achieved Cre-induced, cell-specific deletion and functional
360 analysis of targeted genes in both embryos and adult hearts. Therefore, our CRISPR-
361 based Zwitch method can be widely applied for generating conditional mutant
362 zebrafish in particular and possibly extended for other animal mutants in general.
363
364 Development of the vasculature in the central nervous system can be classified into
365 three phases: vasculogenesis, angiogenesis and blood-brain barrier formation. The
366 hallmark of CNS vasculature maturation is acquisition of BBB properties,
367 establishing a stable environment crucial for brain homeostasis in response to
368 extrinsic factors and physiological changes. The core features of the BBB include
369 specialized tight junctions, highly selective transporters and limited immune cell
370 trafficking [48,49]. In zebrafish, BBB can be functionally characterized from 3 dpf [50,51].
371 While *bubblehead* mutants acquire vessel rapture phenotype early before BBB
372 maturation, presenting a good hemorrhagic model for studying early BBB

373 development. Multiple types of cells contribute to diverse aspects of BBB
374 development and maintenance, leading to proper vasculature function across
375 developmental timeline. Pericytes are perivascular cells embedded within the same
376 basement membrane with endothelial cells [52]. Pericyte-deficient mice with disrupting
377 PDGF-B signaling displayed BBB leakiness, reflecting altered pericyte coverage and
378 endothelial gene expressions [53-55]. Pericyte-secreted signals promoting the endothelial
379 survival, proliferation and sprout formation *via* multiple pathways such as
380 transforming growth factor-β (TGF-β) signaling [56-59], VEGF-VEGFR signaling [60,61],
381 Angiopoietin-Tie2 signaling [62-64], Sphingosine-1-phosphate (S1P) signaling [65] and
382 Notch signaling [66,67]. Apart from endothelial cells, pericytes also regulate
383 development of other members of the neurovascular unit. Pericytes regulate astrocyte
384 aquaporin-4 polarization and guide end-foot processes toward endothelial tubes [53,68].
385 In addition, pericytes secrete ECM molecules supporting the basement membrane and
386 regulation of the angioarchitecture [69-72].
387
388 Endothelial cells form the continuous inner layer of blood vessels with junctional
389 protein and selective transporters, which are the main subject of permeability
390 regulation in BBB. It is well accepted that endothelial cells do not show a
391 predetermined role and that the brain environment is sufficient to induce endothelial
392 barrier [73]. Accumulative evidences also point to critical role of endothelial signals in
393 regulating several aspects of BBB development. In particular, endothelial cell-derived
394 PDGF-B directly binds to surface receptor PDGFRβ on pericytes that are critical for

395 pericyte recruitment and function [74,75]. Although their barrier properties are non-
396 assessed, angiocrine signals such as leukaemia inhibitory factor (LIF) and TGF-β
397 induce both astrocyte [76] and oligodendrocyte differentiation [77], respectively. Wnt7a/b
398 ligands secreted by neural progenitor cells bind to Frizzled receptors on endothelial
399 cells, activating canonical Wnt signaling and downstream genes. WNT ligands
400 knockouts lead to angiogenic defects and BBB leakages specifically in the CNS [78].
401 Endothelial GPR124, as a coactivator of canonical Wnt signaling, has important
402 function in CNS-specific angiogenesis and BBB establishment [79-81]. Other signaling
403 ligands such as angiopoietins and Ephrin family ligands orchestrate with Tie or EphB
404 receptors on endothelial cells, respectively[82]. Briefly, complex interactions between
405 BBB cell types orchestrate proper angiogenesis and CNS development in a spatio-
406 temporal manner.
407
408 Compared with pericytes and endothelial cell signaling, we have less knowledge on
409 glia signaling in the BBB development and maturation. Astrocytes ensheathe
410 capillaries through polarized end feet that are enriched with aquaporin-4 (Aqp4)
411 proteins, colocalized with inwardly rectified K^+ channels[83,84]. Functional coupling of
412 ion and water fluxes plays a critical role in regulating local osmotic
413 equilibrium. During development, radial glia is a neuroepithelial origin with
414 heterogeneous populations that are able to generate neurons, astrocytes, and
415 oligodendrocytes[85-88]. In zebrafish, radial glia has long been considered serving an
416 astrocytic role. Radial glia in zebrafish enriches with several key molecular markers

417 for astrocytes and tight junctions while Aqp4^{+} radial glial processes rarely contact the
418 vasculature[89]. A more recent article has reported that zebrafish *Glast*-expressing radial
419 glia transform into astrocyte-like cells, displaying dense cellular processes, tiling
420 behavior and proximity to synapses [90]. Whether end feet of these astrocytes enwrap
421 capillary blood vessels and resemble mammalian astrocytes warranty future
422 investigations. In agreement with mammalian astrocytes, two independent groups
423 have shown that ablation of pan-glia results in progressive brain hemorrhage[91,92] or
424 deficiency of spinal cord arteries development in zebrafish [93], demonstrating
425 important role of zebrafish glia in BBB formation. Multiple glia/astrocyte-derived
426 signals have been shown to contribute to endothelial barrier properties development.
427 Astrocyte-expressed sonic hedgehog (Shh) bind to hedgehog (Hh) receptors on
428 endothelial cells and contribute to the BBB functions by promoting junctional protein
429 expression and the quiescence of the immune system [94-97]. Before BBB formation,
430 notochord-derived Shh activity promote arterial cell fate on developing endothelial
431 cells [98]. Shh stimulates the production of angiogenic cytokines, angiopoietins and
432 interleukins, *via* downstream transcription factor *Gli* or non-canonical pathways
433 crosstalks with iNOS/Netrin-1/PKC, RhoA/Rock, ERK/MAPK, PI3K/Akt, Wnt/β-
434 catenin, and Notch signaling pathways [99]. VEGF is the main pro-angiogenic growth
435 factor produced by various cell types that controls multiple vascular development
436 steps, such as proliferation, migration, permeability and survival *via* interacting with
437 VEGF receptors on endothelial cells. Inactivation of VEGFA in astrocytes leads to
438 BBB disruption in multiple sclerosis models [100,101]. In early development of avascular

439 neural tube, VEGF derived from neuroectoderm serve as a central role in inducing tip
440 cells sprouting from the perineural vascular plexus (PVNP) and formation of
441 vasculature lumens from stem cells [102,103]. Ablating neuroglia reduces *vegfab* signals
442 and leads to ectopic intersegmental vessels sprouting and vertebral arteries in
443 zebrafish [93]. VEGF signaling orchestrates elaborately with other signaling pathways
444 such as delta-like 4 (Dll4)/Notch signaling [104] and activates downstream components
445 including the Ras/Raf/MEK, PI3K/AKT, and p38/MAPK/HSP27 pathways [105]. Our
446 data suggest glial *betaPix* as an important factor in vascular integrity development.
447 Together with previous studies, *betaPix-Pak1-stathmin* signaling regulates glial
448 growth and differentiation[32] and betaPix regulates *Vegfaa* secretion *via* downstream
449 transcription factors *Zfhx3/4*. Thus, this work presents a novel glial betaPix signaling
450 in regulating zebrafish BBB development.
451
452 Basement membrane is a non-cellular component consisting of several extracellular
453 matrix (ECM) proteins, which laminins are the most abundant ones, while collagen
454 IV, fibronectin, and perlecan serve as hub for structural supports, anchoring and
455 intercellular communication. Components of basement membrane are synthesized in
456 surrounding cells with diverse expression patterns [106]. For example, mice with
457 deletion of Collagen IV in either brain microvascular endothelial cells (BMEC)- or
458 pericytes lead to fully penetrant intracerebral haemorrhage, while COL4A1 deletion
459 in astrocytes results in mild haemorrhage phenotypes [69]. Differential cell-specific
460 expression pattern of laminin isoforms contribute differently to BBB formation [107]. As

461 astrocytic laminins mediate pericyte differentiation and regulate capillary
462 permeability [108], intercellular interactions with the ECM occur by cell surface integrin
463 receptors. Integrin β1 on endothelial cells are critical during angiogenesis[109]. On the
464 other hand, integrin αvβ8 has glial-specific enrichment which mediate focal adhesion
465 to modulate vascular integrity[17,110,111]. Notably, degradation of ECM and focal
466 adhesions at the perivascular space is responsible for the hemorrhagic phenotypes of
467 *bbh* mutants [17,18]. It would be of great interest to determine whether glial *betaPix*
468 account for ECM breakdown in *bbh* mutants in future studies.
469

Acknowledgements

The authors thank Drs. Bo Zhang, Jiulin Du, Liangyi Chen, Kazu Kikuchi, and Jian Chen for providing fish lines, plasmid clones, and human glial cell lines; the members of Dr. Jing-Wei Xiong's laboratory for helpful discussions and technical assistance; and the National Center for Protein Sciences at Peking University, particularly Dr. Liying Du at the Flow Cytometry Core for technical help on the Beckman Coulter MoFlo XDP; and Dr. Hua Liang at National Biomedical Imaging Center, Peking University for assistance with the Luxendo Multi-View Selective-Plane Illumination Microscopy (Bruker). This work is supported by grants from the National Key R&D Program of China (2019YFA0801602 and 2023YFA1800600); the National Natural Science Foundation of China (32230032 and 31730061).

Declaration of Interest

The authors declare no competing financial interests.

485 **Materials and Methods**

486 **Fish maintenance**

487 Zebrafish were raised and handled in accordance with the guidelines of the Peking
488 University Animal Care and Use Committee accredited by the AAALAC.

489 The *bbh*^{fn40a} mutant was isolated from a large-scale mutagenesis screen of the zebrafish
490 genome at Massachusetts General Hospital, Boston[9]. Tg(*acta2:GFP-Cre*) was
491 purchased from Xinjia Pharmaceutical Technology Co., Ltd (Nanjing, China);
492 Tg(*neurod:EGFP*) were kindly provided by Dr. Bo Zhang (Peking University, China);
493 Tg(*huC:GFP*) were kindly provided by Dr. Liangyi Chen (Peking University, China);
494 Tg(*kdrl:GFP*) [112] and Tg(*kdrl:mCherry*) [113] were described previously.

495

496 **Cell culture and transfection**

497 U251 and A172 human glioblastoma cell lines, kindly provided by Dr. Jian Chen at
498 Chinese Institute for Brain Research, Beijing, were cultured in high glucose DMEM
499 medium (Hyclone) supplemented with 10% fetal bovine serum and 1%
500 penicillin/streptomycin, at 37°C in 5% CO_2 humidified incubator. The *betaPix* siRNAs
501 and *STMN1* siRNAs were purchased from GenePharma (Shanghai, China). The
502 sequences of the siRNAs are listed in **Table S2**. Transfection was conducted with
503 Lipofectamine 3000 (Invitrogen) at a final siRNA concentration of 30 nM.

504

505 **mRNA/gRNA synthesis and microinjections**

506 mRNA and gRNA were synthesized as described previously [114]. In brief, linearized

507 pT3TS-nls-zCas9-nls [115], pXT7-*Cre*, and pXT7-*Zfhx4* plasmid DNA were purified as
508 templates using TIANquick Mini Purification Kit (TIANGEN, DP203, China). Next,
509 *in vitro* transcription reactions were performed using the mMESSAGE mMACHINE
510 T3 (for pT3TS-nls-zCas9-nls) or T7 (for pXT7-*Cre* and pXT7-*Zfhx4*) kits (Life
511 Technologies) according to manufacturer's instructions. Templates for gRNA were
512 generated by complementary annealing and elongation of two oligos. Forward oligo
513 contained a T7 promoter and gRNA target sequence, and reverse oligo contained the
514 universal gRNA scaffold [23]. The resulting double-stranded DNA served as the templates
515 for *in vitro* transcription using HiScribe® T7 High Yield RNA Synthesis Kit (NEB).
516 The sequences of the gRNAs are listed in **Table S3**. For global *betaPix* inactivation,
517 *Cre* mRNA with a working concentration of 200 ng/μL were injected into the *betaPix*$^{ct/ct}$
518 embryos at one-cell stage. For CRISPR-mediated knockouts, 300 ng/μL Cas9 mRNA
519 and 20-50 ng/μL gRNAs were injected into zebrafish embryos at one-cell stage. For
520 *Zfhx4* rescue experiments, *Zfhx4* mRNA with a working concentration of 400 ng/μL
521 were injected into the *bbh*^{fn40a} mutants or in combination with CRISPR-mediated
522 *betaPix* knockout system at one-cell stage. Injected embryos were scored for mutant
523 phenotypes at 36 or 48 hpf.
524

525 **Construction of *betaPix* conditional knockout zebrafish**

526 The pZwitch plasmid clone was kindly provided by Dr. Kazu Kikuchi (National
527 Cerebral and Cardiovascular Center Research Institute, Suita, Japan). GSG spacer was
528 added to pZwitch+3 between P2A and TagRFP coding sequences by overlapping primer

529 pairs. Next, a highly efficient gRNA was found from the fifth intron of *betaPix*. Primer
530 pairs were designed to amplify the left and right homologous arms from the gRNA site
531 for 1000 bp and 24 bp with following modifications: 1) The 5' end of the forward primer
532 of the left homologous arm were added with an *Nhe*1 site and a universal gRNA site
533 which provided an *in vivo* linearization cleavage site; a *Mlu*1 site to the 5' end of the
534 reverse primer of the left arm. 2) Added *EcoR*1 site to the 5' end of the forward primer
535 of the right homologous arm; added *Xho1* site and universal gRNA site to the 5' end of
536 the reverse primer of the right homologous arm. Then we cloned the inverted
537 homologous arms into polyclonal sites of the modified pZwitch+3, and purified plasmid
538 DNA with EndoFree Mini Plasmid Kit (Tiangen, DP118). *In vivo* knock-in system was
539 composed of 300 ng/μL Cas9 mRNA, 50 ng/μL *betaPix*-intron5 gRNA, 50 ng/μL
540 Universal gRNA, and 20 ng/μL donor vector. Microinjected *in vivo* knock-in system
541 into wildtype embryos at one-cell stage. Fish founders were screened for *α*-crystallin
542 reporter expression, raised to adulthood, and re-screened for germline transmission and
543 precise knock-in by Sanger sequencing.
544

545 **Construction of transgenic reporters**

546 The glial reporter plasmid *gfap*-EGFP [26] was kindly provided by Dr Jiulin Du (Shanghai
547 Institute for Biological Sciences, Shanghai, China). The *gfap* promoter was used to
548 establish Tg(*gfap:GFP-Cre*) plasmid. The *stmn1b* coding sequences were amplified
549 from wild-type zebrafish cDNA library, which were used to establish Tg(*gfap:GFP-*
550 *stmn1b*) plasmid.

551 Transgenic reporters were generated by using *Tol2*-based transgenesis [116]. In brief, 100
552 ng/μL *Tol2* transposase mRNA in combination with 20 ng/μL donor plasmid DNA were
553 co-injected into the embryos at one-cell stage. Transgenic founders were screened
554 for specific transgenic GFP expression, raised to adulthood, and re-screened for
555 germline transmission.
556
557 **Inhibitor treatment**
558 IPA-3 (Proteintech, CM05727) were dissolved in DMSO to form a 10 mM stock, and
559 then diluted with E3 medium to 3 μM in 6-well plates. Zebrafish embryos were treated
560 from 24 to 48 hpf, and then washed with E3 medium for phenotype analysis.
561
562 ***o*-dianisidine staining**
563 *o*-dianisidine staining was performed as described previously [18]. In brief, embryos were
564 dechorionated, anesthetized and incubated in fresh staining solution (0.6 mg/mL *o*-
565 dianisidine, 0.01 M sodium acetate pH4.5, 0.65% H_2O_2 and 40% Ethanol) for 20
566 minutes in dark. Washed three times with methanol, and performed benzyl
567 alcohol/benzyl benzoate (BABB) tissue clearing before imaging with stereo
568 microscope (Leica, 160F).
569
570 **Whole-mount *in situ* hybridization (WISH)**
571 Whole-mount *in situ* RNA hybridization was performed as described previously [117].
572 Antisense probes were synthesized using a digoxigenin RNA labeling kit (Roche,

573 11277073910). Primer sequences for all WISH probes used in this paper are provided
574 in **Table S4**.
575
576 **Quantitative real-time RT-PCR**
577 Total RNA was isolated from embryos using Trizol (invitrogen) and cDNA was
578 generated using HiScript® III RT SuperMix (Vazyme) according to the manufacturer's
579 instruction. Quantitative real-time PCR was performed using Lightcycler (Roche) and
580 ChamQ SYBR qPCR Master Mix (Vazyme). Primer sequences are listed in
581 Supplementary Materials **Table S5**. Gene expression level was normalized against
582 GAPDH level.
583
584 **Light-sheet fluorescence microscopy imaging**
585 Light-sheet microscopy imaging was performed as described previously [118]. In brief,
586 transgenic zebrafish embryos were collected and maintained at 28.5°C. At the required
587 developmental stages, the embryos were carefully dechorionated, paralyzed with
588 tricaine, and transferred into 1% ultrapure low melting point agarose (16520-050;
589 Invitrogen). The embryo was then drawn into a glass tube in top-down position using a
590 1 mL syringe with an 18G blunt needle. After agarose coagulation, a wire was inserted
591 from bottom to push the agarose with embryo upwards, removed excess agar until the
592 head area is exposed from the top of the glass tube. Finally, the glass tube was fixed in
593 a sample holder for subsequent imaging.
594 Imaging was carried out with Luxendo Multi-View Selective-Plane Illumination

595 Microscopy (Bruker). Optical calibrations were adjusted according to the instruction
596 manual.
597 The optical plates are emitted from two Nikon CFI Plan Fluor 10x W 0.3 NA immersion
598 objectives in opposite directions. The detection is completed by two Olympus 20x 1.0
599 NA immersion lenses. The parameters are set as follows: the green fluorescence channel
600 uses a laser of 488 nm coupled with BP497-554 filter, the red fluorescent channel uses
601 laser 561 nm coupled with BP580-627 filter, with an exposure time of 100 ms, a delay
602 of 11 ms, a line mode of 50 px, and z-Stack interval of 3 μm. The raw data were stored
603 in H5 file format, processed into TIFF format and merged Multi-View dataset using
604 MATLAB software. After pre-processing, multi-fluorescence channels were merged in
605 ImageJ, and 3D visualization and measurement were performed by Imaris.
606
607 **Single-cell RNA sequencing**
608 For knockout samples, 300 ng/μL Cas9 mRNA and a mixture of number 1 to 4 *betaPix*
609 gRNAs with 50 ng/μL each were co-injected into wildtype embryos at one-cell stage.
610 Injection with equivalent concentration of Cas9 mRNA with PBS served as siblings.
611 After microinjection, embryos were collected and maintained at 28.5°C. At 24 or 48
612 hpf, zebrafish were dechorionated, paralyzed and transferred onto agarose plate. Heads
613 were harvested with dissecting scissors in cold sterile 1X PBS with pooling 200 heads
614 for each group. Heads were then dissociated in 900 μL Accutase cell detachment
615 solution (Sigma-Aldrich, A6964) at 28.5°C for 3 hours and re-suspended by pipetting
616 every 30 min. Once digestion was complete, 100 μL FBS was added to cell suspension

617 and centrifuged at 4℃, 500 g for 3 min. The cells were gently re-suspended in cold 500
618 μL 2.5% FBS in 1X PBS and filtered through a 40 μm strainer. PI and Hoechst33342
619 were stained for distinguishing living cells. The single, living cells were sorted by Aria
620 SORP (BD biosciences) into 1.5 ml tubes. The cell counts and vitality were verified by
621 AOPI staining coupled with an Automated Cell Counter (Countstar BioTech). Single
622 cells were barcoded with Chromium Next GEM Single Cell 3 'Reagent Kits V3.1 kit
623 (10x Genomics, 1000269) in 10× Chromium Controller (10× Genomics). After
624 qualified by peak shapes, fragment size and tailing with Fragment Analyzer System kit
625 (Agilent Technologies, DNF-915), single-cell transcriptome libraries were sequenced
626 via Illumina High Throughput Sequencing PE150 (Novogene, Beijing). The sequencing
627 data were analyzed using the CellRanger-6.1.1 (10x Genomics) and mapped to
628 reference genome GRCz11-GRCz11.103.
629 Cells were excluded from subsequent analyses under the following conditions: when
630 the number of expressed genes was less than 500, when there were abnormally high
631 counts of UMIs or genes (outliers of a normal distribution), or when the mitochondrial
632 content exceeded 9%. Unsupervised clustering was performed using Seurat (version:
633 4.0.2) with a resolution of 2.5, resulted in 71 cell populations and further annotated into
634 24 zebrafish major cranial cell types. Differential expression analysis in Seurat v4 was
635 used to identify cluster/cell type markers by Wilcoxon rank sum test.
636
637 **Scratch assay**
638 U251 cells were planted into culture plate and performed transfection at the desired

density. At 24 hours post-transfection, we vertically scratched monolayer cells by using a 200 μL pipette tip. Washed the cells three times with PBS, then replaced with serum-free culture medium for further culture. Stereo fluorescence microscopy (Leica, 160F) was used to document the scratch size at 0 hours, 18 and 24 hours. Images were processed by ImageJ.

Immunostaining

For assessing tubulin expression, U251 cells were planted into chamber slides (Saining, 1093000) and transfected at the desired density. At 24 hours post-transfection, washed the cells once on ice with pre-cooled PBS, then fixed with pre-cooled methanol at -20℃ for 20 minutes. The fixed cells were permeabilized with pre-cooled acetone at -20℃ for 1 minute. Removed acetone, incubated 0.5% BSA/PBS blocking solution at room temperature for 15 minutes. Cells were then incubated with 1:200 anti-α-tubulin mouse monoclonal antibody (EASYBIO, BE0031) at 37℃ for 45 minutes. After rinsing once with PBS, cells were incubated with 1:400 Alexa Fluor™ 488 goat anti-mouse IgG (H+L) secondary antibody (Invitrogen, A11029) at 37℃ for another 45 minutes. Washed three times with PBS, and sealed with Mounting Medium with DAPI (ZSGB Bio, ZLI-9557). Images were acquired by upright fluorescence microscopy (Leica, DM5000B) at 40× magnification, and processed by ImageJ.

Statistical analysis

Statistical analysis was performed using Graphpad Prism 6. The statistical significance

661 of differences between the two groups was determined by the independent unpaired
662 Student's t-test. Among three or more groups, one-way ANOVA analysis coupled with
663 Dunnett's test were used. All data are presented as the mean ± SEM. P value <0.05
664 indicates significant, with individual P values mentioned in the figure/figure legends.
665

666 **Figure Legends**

667 **Figure 1. Generation of *betaPix* conditional trap (*betaPix*^{ct}) allele by an**

668 **homologous recombination (HDR)-mediated knock-in method.**

669 (A) Schematic diagram illustrates the HDR-mediated *Zwitch* strategy for

670 generating zebrafish knock-in allele at the *betaPix* locus.

671 (B) Genomic PCR analysis of the F_1 embryos confirming the right *Zwitch*

672 insertions.

673 (C) Sanger sequencing confirming the junction of *betaPix*^{ct} (after HDR-mediated

674 insertion) or *betaPix*^{m} (after Cre-mediated inversion) that are highlighted by

675 RED lines in (A).

676 (D) Representative stereomicroscopy images of erythrocytes stained with o-

677 dianisidine in *betaPix*$^{ct/ct}$ and *betaPix*$^{m/m}$ embryos at 48 hpf. Brain

678 hemorrhages, indicated with arrows, in Cre mRNA-injected embryos

679 (*betaPix*$^{m/m}$). Lateral views, anterior to the left.

680 (E) Quantification of hemorrhagic parameters in (D). Left panel showing

681 hemorrhage percentages with each dot representing an individual experiment

682 (n>100 each), and right panel showing hemorrhage areas with each dot

683 representing one embryo.

684 (F) qRT-PCR analysis showing the expression of *betaPix*, *RFP* and *alphaPix* in

685 *betaPix*$^{ct/ct}$, *betaPix*$^{ct/m}$, and *betaPix*$^{m/m}$ embryos at 48 hpf. Each dot represents

686 one embryo. cryaa, αA-crystallin; PA, polyadenylation signal; SA, splice

687 acceptor; T2A, T2A self-cleaving peptide.

688 **Figure 2. *betaPix*$^{m/m}$ mutant have brain hemorrhages, central artery defects and**
689 **abnormal glial structure that was partially rescued by Pak1 inhibitor IPA3**
690 **treatment.**

691 (A) Left panel showing the maximum intensity projection of the glial structures in
692 the hindbrain of *betaPix*$^{ct/ct}$ and *betaPix*$^{m/m}$ embryos at 48 hpf. Lateral view,
693 anterior to left. Middle panel showing representative optical sections and right
694 panel showing the higher magnifications of boxed area, presenting atypical
695 glial structures with disoriented arrangements (yellow arrows) in *betaPix*$^{m/m}$
696 embryos.

697 (B) Quantification of glial parameters in (A). Left panel showing the average glia
698 length, and right panel showing glia length index normalized to individual
699 head length, which each dot represents one embryo.

700 (C) Whole-mount RNA *in situ* hybridization revealed *nestin* and *pax2a* expression
701 pattern in *betaPix*$^{ct/ct}$ and *betaPix*$^{m/m}$ embryos at 48 hpf. Dorsal view, anterior
702 to the left.

703 (D) Optical sections of glial structure (green) and blood vessels (magenta) in the
704 heads of siblings and CRISPR-mediated *betaPix* F_0 knockout embryos.
705 Arteries in the hindbrain of *betaPix* KO mutants had developmental defects
706 (white arrowheads), showing shorter distance between basilar artery (BA) and
707 glial cell bodies.

708 (E) 3D reconstruction of the sox2-positive precursors (green) and vasculatures
709 (magenta) in the heads of siblings and CRISPR-mediated *betaPix* F_0 knockout

710 embryos at 48 hpf. Box areas are shown in higher magnifications at the middle
711 panels, with optical sections shown in the right panels. Arrows indicate CtA
712 with enlarged perivascular space.
713 (F) Representative stereomicroscopy images of *o*-dianisidine staining of
714 *betaPix*$^{ct/ct}$ and *betaPix*$^{m/m}$ embryos at 48 hpf that were treated with DMSO or
715 PAK inhibitor IPA3. Brain hemorrhages indicated with the arrows.
716 (G) Quantification of brain hemorrhagic parameters in (F).
717 (H) 3D reconstruction of the glial structure (green) and vasculature (magenta) in
718 the heads of *betaPix*$^{ct/ct}$ and *betaPix*$^{m/m}$ embryos at 48 hpf treated with DMSO
719 or IPA3. Lateral view, anterior to left. Defects in CtAs (white arrows) and glia
720 (yellow arrows) shown in *betaPix*$^{m/m}$ embryos treated with DMSO or IPA3.
721 (I) Quantification of CtA parameters in (H).
722 (J) Quantification of glia parameters in (H).
723
724 **Figure 3. Glial-specific *betaPix* knockouts recapture global *betaPix* mutant**
725 **phenotypes.**
726 (A) Representative stereomicroscopy images of erythrocytes stained with *o*-
727 dianisidine in *betaPix*$^{ct/ct}$ siblings and *gfap:GFP-Cre*; *betaPix*$^{ct/ct}$ mutant
728 embryos treated with DMSO or IPA3 at 48 hpf. Brain hemorrhages indicated
729 with arrows in glial-specific *betaPix* knockouts. Lateral view with anterior to
730 the left.

731 (B) 3D reconstruction of the vasculatures (magenta) in the heads at 48 hpf,
732 showing lateral view with anterior to the left. The box areas are shown in
733 higher magnifications of brain vasculatures at the right panels. CtA defects
734 (yellow arrows) were evident in *gfap:GFP-Cre*; *betaPix*$^{ct/ct}$ mutant embryos.
735 (C) Quantification of brain hemorrhages (A) and CtA parameters (B). Left panel
736 showing hemorrhage percentages with each dot representing an individual
737 experiment (n>100 each). Middle panel showing hemorrhage areas with each
738 dot representing one embryo. Right panel showing CtA length index
739 normalized to individual head length, with each dot representing one embryo.
740

741 **Figure 4. Single cell transcriptome reveals that a subcluster of glial progenitor and**
742 **stathmin family members are associated with *betaPix* mutation.**
743 (A) Experimental strategy for single cell RNA sequencing of embryonic heads
744 from wild-type siblings and *betaPix* CRISPR mutants at 1 dpf and 2 dpf.
745 (B) UMAP visualization and clustering of cells labeled by cell type. Four samples
746 were aggregated and analyzed together.
747 (C) Proportions of 24 cell clusters were differentially distributed among four
748 sample groups. ctrl_1d, PBS-injected siblings at 1 dpf; ko_1d, *betaPix*
749 CRISPR mutants at 1 dpf; ctrl_2d, PBS-injected siblings at 2 dpf; ko_2d,
750 *betaPix* CRISPR mutants at 2 dpf.
751 (D) Enriched GO terms for differentially expressed genes for progenitor sub-
752 cluster comparing ko_2d to ctrl_2d groups.

753 (E) Violin plots showing the expression of the stathmin family genes by all cells
754 among four sample groups (left panel) or by progenitor sub-cluster among
755 four sample groups (right panel).
756 (F) qRT-PCR analysis showing expression of *betaPix*, *stmn1a*, *stmn1b*, *stmn4l* and
757 *ppfia3* in glia of FACS-sorted *betaPix*$^{ct/ct}$ siblings and *betaPix*$^{m/m}$ mutants at 48
758 hpf. Each dot represents cells sorted from one embryo.
759 (G) qRT-PCR analysis showing expression of *betaPix*, *stmn1a*, *stmn1b*, *stmn4l* and
760 *ppfia3* in glia of FACS-sorted *betaPix*$^{ct/ct}$ siblings and *gfap:GFP-Cre*;
761 *betaPix*$^{ct/ct}$ mutants at 48 hpf. Each dot represents cells sorted from one
762 embryo.
763 (H) Whole-mount RNA *in situ* hybridization revealing down-regulation of *stmn1a*,
764 *stmn1b* and *stmn4l* in *betaPix*$^{ct/ct}$ siblings and *gfap:GFP-Cre*; *betaPix*$^{ct/ct}$
765 mutant embryos at 48 hpf.
766
767 **Figure 5. Stathmin acts downstream of *betaPix* in glial migration *via* regulating**
768 **tubulin polymerization.**
769 (A) Whole-mount RNA *in situ* hybridization showing that *stmn1a, stmn1b and*
770 *stmn4l* expression in *gfap:GFP-Cre*; *betaPix*$^{ct/ct}$ embryos were partially
771 rescued by Pak1 inhibitor IPA3 treatment at 48 hpf. Dorsal views, anterior to
772 the left.

773 (B) qRT-PCR analysis showing that *stmn1a* and *stmn4l* expression were rescued in
774 *gfap:GFP-Cre*; *betaPix*$^{ct/ct}$ mutants by IPA3 treatment at 48 hpf. Each dot
775 represents one embryo.
776 (C) Representative stereomicroscopy images of erythrocytes stained with *o*-
777 dianisidine in siblings and *stmn1a/1b/4l* CRISPR mutants at 48 hpf. Brain
778 hemorrhages, indicated with arrows, appeared in *stmn1a/1b/4l* mutants.
779 Lateral views with anterior to the left.
780 (D) Quantification of hemorrhagic parameters in (C). Left panel showing
781 hemorrhage percentages with each dot representing an individual experiment
782 (n>100 each), and right panel showing hemorrhage areas with each dot
783 representing one embryo.
784 (E) 3D reconstruction of glial structure (green) and vasculature (magenta) in the
785 heads at 48 hpf. Lateral view with anterior to the left. CtA defects (white
786 arrows) appeared in *stmn1a/1b/4l* mutants.
787 (F) Quantification of CtA and glia parameters in (E). Length index normalized to
788 individual head length, with each dot representing one embryo.
789 (G) Representative stereomicroscopy images of erythrocytes stained with *o*-
790 dianisidine in *bbh*^{fn40a} and *bbh*^{fn40a}; Tg(*gfap:GFP-stmn1b*) embryos at 48 hpf.
791 Brain hemorrhages, indicated with arrows, decreased in *bbh*^{fn40a} mutants with
792 glia-specific overexpression of *stmn1b*, compared with *bbh*^{fn40a} mutant
793 siblings. Lateral views with anterior to the left.

794 (H) Quantification of hemorrhagic parameters of (G). Left panel showing
795 hemorrhage percentages with each dot representing an individual experiment
796 (n>100 each), and right panel showing hemorrhage area with each dot
797 representing one embryo.
798 (I) 3D reconstruction of the *gfap:GFP-stmn1b* overexpression (green) and
799 vasculature (magenta) in the heads of *bbh*^{fn40a} siblings and *bbh*^{fn40a};
800 Tg(*gfap:GFP-stmn1b*) mutants at 48 hpf. Lateral view with anterior to
801 left. White arrows indicate CtA defects.
802 (J) Quantification of CtA and glia parameters in (I). Length index normalized to
803 individual head length, with each dot representing one embryo.
804 (K) Representative stereomicroscopy images of U251 cells at 0 and 24 hours after
805 wounding. U251 cells were transfected with negative control siRNA or *betaPIX*
806 siRNA separately, in combination with pcDNA3.1 vector, *betaPIX*
807 overexpression plasmid, and *STMN1* overexpression plasmid. The wound edges
808 are highlighted by dashed lines, with arrow lines indicating the wound width.
809 (L) Quantification of wound closure in (K), showing $^{*}P<0.05$, $^{***}P<0.005$
810 compared to negative control siRNA with empty vector transfection. $^{\#\#}P<0.01$,
811 $^{\#\#\#}P<0.005$ compared to *betaPix* knockdown with empty vector transfection.
812 (M) Representative immunofluorescence image of alpha-tubulin and DAPI
813 signals in U251 cells. U251 cells were transfected with negative control
814 siRNA or *betaPIX* siRNA separately, in combination with pcDNA3.1 vector,
815 *betaPIX* overexpression plasmid, and *STMN1* overexpression plasmid. Box

816 areas are shown in higher magnifications. Arrows indicate protrusions at the
817 cell periphery.
818 (N) Quantification of cell percentages with protrusions in (M). $^{***}P<0.005$
819 compared to negative control siRNA with empty vector transfection. $^{\#}P<0.05$,
820 $^{\#\#}P<0.01$ compared to *betaPix* knockdown with empty vector transfection.
821
822 **Figure 6. *Zfhx3/4* acts downstream of *betaPix* to regulate vascular integrity**
823 **development.**
824 (A) Whole-mount RNA *in situ* hybridization revealing that *vegfaa* decreased in
825 *bbh*^{fn40a} mutants compared with siblings at 36 hpf. Lateral views with anterior
826 to the left. Arrows indicate *vegfaa* expression in the CtAs.
827 (B) qRT-PCR analysis revealing that *ZFHX3*, *ZFHX4 and* VEGFA decreased in
828 U251 cells transfected with *betaPIX* siRNA, which were rescued by *betaPIX*
829 overexpression.
830 (C) Whole-mount RNA *in situ* hybridization showing that *vegfaa* decreased in
831 CRISPR-mediated *zfhx3/4* F_0 knockout embryos at 36 hpf. Lateral views with
832 anterior to the left. Arrows indicate *vegfaa* expression in the CtAs.
833 (D) Representative stereomicroscopy images of erythrocytes stained with *o*-
834 dianisidine in siblings and CRISPR-mediated *zfhx3/4* F_0 knockout embryos at
835 48 hpf. Arrows indicated brain hemorrhages in the knockout brains. Lateral
836 views with anterior to the left.

837 (E) Quantification of hemorrhagic parameters in (D). Left panel showing
838 hemorrhage percentages with each dot representing an individual experiment
839 (n>100 each), and right panel showing hemorrhage areas with each dot
840 representing one embryo.
841 (F) 3D reconstruction of the glial structure (green) and vasculature (magenta) in
842 the hindbrains of siblings and CRISPR-mediated *zfhx3/4* F_0 knockouts at 48
843 hpf. Lateral view with anterior to the left. White arrows indicate CtA defects
844 in *zfhx3/4* knockout embryos.
845 (G) Quantification of CtA and glia length parameters of (F). Length index
846 normalized to individual head length, with each dot representing one embryo.
847 (H) Representative stereomicroscopy images of erythrocytes stained with *o*-
848 dianisidine in CRISPR-mediated *betaPix* F0 knockout embryos with or
849 without *zfhx4* mRNA injection at 48 hpf. Arrows indicate brain hemorrhages.
850 Lateral views with anterior to the left.
851 (I) Quantification of hemorrhagic parameters in (H). Left panel showing
852 hemorrhage percentages with each dot representing an individual experiment
853 (n>100 each), and right panel showing hemorrhage area with each dot
854 representing one embryo.
855 (J) 3D reconstruction of the glial structure (green) and vasculature (magenta) in
856 CRISPR-mediated *betaPix* F_0 knockout embryos with or without *zfhx4* mRNA
857 injection at 48 hpf. White arrows indicate CtAs and yellow arrows indicate
858 glia.

859 (K) Quantification of CtA and glia length parameters in (J). Length index
860 normalized to individual head length, with each dot representing one embryo.
861 (L) Whole-mount RNA *in situ* hybridization revealed that *zfhx4* and *vegfaa*
862 decreased in CRISPR-mediated *betaPix* F_0 knockout embryos at 36 hpf, which
863 were rescued by *zfhx4* mRNA injection. Lateral views with anterior to the left.
864 Arrows indicate hindbrain regions.
865 (M) Dot plots of several angiogenesis-associated genes expression in endothelial
866 cell cluster. Dot size indicates the percentage of cells with gene expression, and
867 dot color represents the average gene expression level.
868
869 **Figure 7. Working Model on the function of glial *betaPix* in zebrafish vascular**
870 **integrity development of the hindbrain.** *betaPix* is enriched in glia and regulates the
871 PAK1-Stathmin axis on microtublin stabilization, thus fine-tuning glial cell migration
872 and their interactions with vanscular endothelial cells; and in paralelle, betaPix may
873 also regulate Zfhx3/4-Vegfaa signaling in glia, which then modulates angiogenesis
874 during cerebral vessel development and maturation. Deletion of *betaPix* affects glial
875 cell migration and interaction with cerebral endothelial cells. MT, Microtubule.
876
877 **Figure S1. Generation of betaPix conditional trap (*betaPix*^{ct}) allele by an HDR-**
878 **mediated knock-in method.**
879 (A) Sanger sequencing results of the original pZwitch (+3) and the modified
880 vector with glycine-serine-glycine spacer (GSG) in front of the 2A peptide.

881 (B) Sanger sequencing results of the genomic PCR products at both junction sites
882 from the *betaPix*^{ct} F_1 offspring showing the correct knock-in in the betaPix
883 locus.
884 (C) The screening process for *betaPix*^{ct} knock-in zebrafish showing about 1%
885 efficiency with correct homologous recombinations.
886 (D) Representative stereomicroscopy images of *o*-dianisidine staining in *bbh*^{fn40a}
887 embryos at 48 hpf. Lateral view, anterior to the left in left panel; Dorsal view,
888 anterior to the top in right panel.
889 (E) Quantification of hemorrhagic parameters in (D). Left panel showing
890 hemorrhage percentages with each dot representing an individual experiment
891 (n>100 each), and right panel showing hemorrhage areas with each dot
892 representing one embryo.
893 (F) 3D reconstruction of the *betaPix* expression (magenta) in *betaPix*$^{ct/+}$ brains of
894 embryos microinjected with PBS or *Cre* mRNA at 24 hpf, 48 hpf, 72 hpf and
895 144 hpf. Cre-induced *RFP* expression indicates successful inversion of gene
896 trap system (arrows). Dorsal view, anterior to the top.
897 (G) 3D reconstruction of the *neurod1* transgenic expression (green) and *betaPix*
898 expression (magenta) in *betaPix*$^{ct/+}$ brains of embryos microinjected with PBS
899 or *Cre* mRNA at 24 hpf, 48 hpf, 72 hpf and 144 hpf. Cre-induced *RFP*
900 expression indicates successful inversion of gene trap system (arrows),
901 marking strong *betaPix* expression at the midbrain hindbrain boundary
902 (MHB), and milder expression at hindbrain at early stages. At 144 hpf, *betaPix*

903 expresses ubiquitously in the brain, outlining the cerebellum (arrowheads).

904 Dorsal view, anterior to the top.

905

906 **Figure S2. *betaPix*$^{m/m}$ mutant had brain hemorrhages, central arteries defects,**

907 **and abnormal glial structure.**

908 (A) 3D reconstruction of the vasculature (green) in the heads with lateral view,

909 anterior to left. Endogenous *betaPix* expression (magenta) only shown in Cre

910 mRNA-injected mutant embryos. The box areas are shown in higher

911 magnifications of vasculatures at the right panels. Central arteries (CtA)

912 defects (white arrows) were evident in *betaPix*$^{m/m}$ embryos at 48 hpf. Arrow

913 lines indicating the CtA length.

914 (B) Quantification of CtA parameters in (A). Left panel showing the average CtA

915 length, and right panel showing the CtA length index normalized to individual

916 head length, with each dot representing one embryo.

917 (C) 3D reconstruction of the glia structure. Box areas showing higher

918 magnifications of glia at the right panels. D, dorsal; V, ventral. Arrow lines

919 indicating the glia length.

920

921 **Figure S3. CRISPR-mediated *betaPix* F_0 knockouts had similar phenotypes as**

922 ***betaPix*$^{m/m}$ mutants.**

923 (A) Schematic diagram illustrates guide RNA sites for CRISPR-mediated *betaPix*

924 F_0 knockout.

925 (B) qRT-PCR revealing that *betaPix* decreased in CRISPR-mediated *betaPix* F_0
926 knockout embryos compared with wild-type siblings at 48 hpf. Each dot
927 represents one embryo.
928 (C) Maximal intensity projection of the glial structure of the hindbrains in siblings
929 and CRISPR-mediated *betaPix* F_0 knockouts at 48 hpf, lateral view with
930 anterior to left.
931 (D) Whole-mount RNA *in situ* hybridization revealing up-regulated *nestin* and
932 down-regulated *pax2a* expression in CRISPR-mediated *betaPix* F_0 knockout
933 embryos at 48 hpf. Dorsal view with the anterior to the left.
934 (E) Quantification of hemorrhagic parameters of siblings and CRISPR-mediated
935 *betaPix* F_0 knockout embryos at 48 hpf. Left panel showing percentages of
936 brain hemorrhage with each dot representing an individual experiment (n>100
937 each), and right panel showing hemorrhage areas with each dot representing
938 one embryo.
939 (F) Quantification of CtA parameters of siblings and CRISPR-mediated *betaPix*
940 F_0 knockout embryos at 48 hpf. Left panel showing average CtA length, and
941 right panel showing CtA length index normalized to individual head length,
942 with each dot representing one embryo.
943 (G) Quantification of glial parameters of siblings and CRISPR-mediated *betaPix*
944 F_0 knockout embryos at 48 hpf. Left panel showing average glia length, and
945 right panel showing glia length index normalized to individual head length,
946 with each dot representing one embryo.

947 **Figure S4. Generating glial-specific *betaPix* knockout zebrafish.**

948 (A) Schematic diagram illustrates establishment of glial-specific *betaPix* knockout
949 zebrafish.

950 (B) 3D reconstruction of the heads at 48 hpf with lateral view, anterior to
951 left. Glial-specific *Cre* expression (green) was only shown in *gfap:GFP-Cre*;
952 *betaPix*$^{ct/ct}$ mutant embryos, which overlaps with betaPix:RFP expression
953 (magenta).

954 (C) Genomic PCR analysis of the *betaPix*^{ct}- or *betaPix*^{m}-unique sequences in
955 *betaPix*$^{ct/ct}$ siblings, *gfap:GFP-Cre*; *betaPix*$^{ct/+}$ heterozygous mutants, and
956 *gfap:GFP-Cre*; *betaPix*$^{ct/ct}$ homozygous mutants.

957 (D) qRT-PCR analysis revealing *Cre* expression in *gfap:GFP*-positive glial
958 population and *gfap:GFP*-negative non-glial population that were sorted from
959 *gfap:GFP-Cre*; *betaPix*$^{ct/ct}$ embryos. Each dot represents one embryo.

960 (E) qRT-PCR analysis showing *betaPix, betaPix-RFP* and *alphaPix* expression in
961 *betaPix*$^{ct/ct}$ control siblings and *gfap:GFP-Cre*; *betaPix*$^{ct/ct}$ mutant embryos at
962 48 hpf. Each dot represents one embryo.

963 (F) Whole-mount RNA *in situ* hybridization revealing that *alphaPix* was
964 comparable but *betaPix* decreased in *gfap:GFP-Cre*; *betaPix*$^{ct/ct}$ *mutants*
965 compared with *betaPix*$^{ct/ct}$ siblings at 48 hpf. Lateral view with anterior to the
966 left.

967

968 **Figure S5. Neither endothelial-, neuronal- nor mural-specific deletion of *betaPix***
969 **caused brain hemorrhages and abnormal CtA phenotypes.**
970 (A) Representative stereomicroscopy images of *o*-dianisidine staining in
971 *betaPix*$^{ct/ct}$, *kdrl:Cre*; *betaPix*$^{ct/ct}$, *huC:GFP-Cre*; *betaPix*$^{ct/ct}$, and *acta2:GFP-*
972 *Cre*; *betaPix*$^{ct/ct}$ embryos at 48 hpf.
973 (B) Quantification of hemorrhage parameters in (A).
974 (C) 3D reconstruction of the vasculature of *betaPix*$^{ct/ct}$, *kdrl:Cre*; *betaPix*$^{ct/ct}$,
975 *huC:GFP-Cre*; *betaPix*$^{ct/ct}$, and *acta2:GFP-Cre*; *betaPix*$^{ct/ct}$ embryos at 48 hpf.
976 Lateral view with anterior to left. The boxed areas of the hindbrains are shown
977 in higher magnifications at the right panels.
978 (D) Quantification of CtA parameters in (C).
979
980 **Figure S6. Glial progenitor sub-cluster of *betaPix* knockouts has down-regulation**
981 **of s*tathmin* family members and up-regulation of *pak1* gene.**
982 (A) UMAP visualization and clustering of cells labeled by cell type across four
983 sample groups.
984 (B) Dot plot of marker genes expression in each cell type. Dot size indicates the
985 percentage of cells expressed, and dot color represents the average expression
986 level.
987 (C) UMAP feature plots displaying relative expression levels of selected
988 transcripts among four sample groups. Cells are colored by expression level.
989

990 **Figure S7. CRISPR-mediated *stmn1a/1b/4l* F_0 knockouts have similar but milder**
991 **phenotypes as *betaPix* knockouts.**

992 (A) qRT-PCR analysis showing that IPA3 treatment rescued *stmn1a* and *stmn4l*
993 expression in CRISPR-mediated *betaPix* F_0 knockouts at 48 hpf. Each dot
994 represents one embryo.

995 (B) Schematic diagram illustrates 4-guide RNAs mediated F_0 knockout strategy in
996 the loci of *stmn1a*, *stmn1b* and *stmn4l*.

997 (C) Whole-mount RNA *in situ* hybridization confirming that *stmn1a, stmn1b* and
998 *stmn4l* decreased in CRISPR-mediated *stmn1a/1b/4l* F_0 knockouts at 48 hpf.
999 Dorsal views with anterior to the left.

1000 (D) qRT-PCR analysis confirming that *stmn1a, stmn1b* and *stmn4l* decreased in
1001 mutant embryos of CRISPR-mediated *stmn1a/1b/4l* F_0 knockouts at 48 hpf.
1002 Each dot represents one embryo.

1003 (E) qRT-PCR analysis confirming that *stmn1a, stmn1b* and *stmn4l* decreased in the
1004 FACS-sorted glia of CRISPR-mediated *stmn1a/1b/4l* F_0 knockouts at 48 hpf.
1005 Each dot represents sorted cells from one embryo.

1006 (F) Optical sections of glial structure in the hindbrains of siblings and CRISPR-
1007 mediated *stmn1a/1b/4l* F_0 knockouts at 48 hpf. Lateral view with anterior to
1008 the left. Abnormal glial structures with disoriented arrangements (yellow
1009 arrows) in *stmn1a/1b/4l* mutant embryos.

1010 (G) Quantification of average CtA and glial length in Figure 5 (E). Each dot
1011 represents one embryo.

1012 (H) Whole-mount RNA *in situ* hybridization revealed that *nestin* increased while
1013 *pax2a* decreased in CRISPR-mediated *stmn1a/1b/4l* F_0 knockout embryos at
1014 48 hpf. Dorsal views with anterior to the left.
1015 (I) 3D reconstruction and whole-mount RNA *in situ* hybridization showing that
1016 *gfap:GFP-stmn1b* transgenic overexpression rescued glial defects in bbh^{fn40a};
1017 Tg(*gfap:GFP-stmn1b*) embryos at 48 hpf. Lateral views with anterior to the
1018 left.
1019 (J) Whole-mount RNA *in situ* hybridization showing that *nestin* and *pax2a* were
1020 normally expressed in bbh^{fn40a}; Tg(*gfap:GFP-stmn1b*) embryos at 48 hpf.
1021 Dorsal views with anterior to the left.
1022 (K) Quantification of average CtA and glia length in Figure 5 (I). Each dot
1023 represents one embryo.
1024 (L) qRT-PCR analysis confirming the efficacy of *betaPix* transgenic over-
1025 expression and *betaPix* siRNA knockdown in U251 cells.
1026 (M) Representative stereomicroscopy images of A172 cells at 0 and 18 hours
1027 after wounding. *betaPIX* siRNA treatment decreased A172 cell migration,
1028 which were rescued by either *betaPIX* or STMN1 overexpression. The wound
1029 edges are highlighted by dashed lines, with arrow lines indicating the wound
1030 width.
1031 (N) Quantification of wound closures in (M). $^{**}P<0.01$ compared to negative
1032 control siRNA and empty vector transfection. $^{\#\#}P<0.01$, $^{\#\#\#}P<0.005$ compared
1033 to *betaPix* knockdown and empty vector transfection.

1034 **Figure S8. *Zfhx3/4* acts downstream of *betaPix* to regulate vascular integrity**
1035 **development.**

1036 (A) Violin plots showing that *zfhx3* and *zfhx4* decreased in progenitor sub-cluster
1037 of *betaPix* knockouts.

1038 (B) qRT-PCR analysis revealing that *zfhx3* and *zfhx4* decreased in FACS-sorted
1039 glia of *gfap:GFP-Cre*; *betaPix*$^{ct/ct}$ mutants compared with *betaPix*$^{ct/ct}$ siblings
1040 at 48 hpf. Each dot represents the cells sorted from one embryo.

1041 (C) Schematic diagram illustrates 4-guide RNAs mediated F_0 knockout strategy in
1042 the *zfhx3* and *zfhx4* loci.

1043 (D) Whole-mount RNA *in situ* hybridization confirming *zfhx3/4* efficiency in
1044 CRISPR-mediated *zfhx3/4* F_0 knockout embryos at 48 hpf.

1045 (E) qRT-PCR analysis revealing that *zfhx3*, *zfhx4*, and *vegfaa* decreased in
1046 CRISPR-mediated *zfhx3/4* F_0 knockout embryos at 36 hpf.

1047 (F) Whole-mount RNA *in situ* hybridization revealing that *nestin* increased in
1048 CRISPR-mediated *zfhx3/4* F_0 knockout embryos at 36 hpf. Arrows indicate the
1049 hindbrain regions.

1050 (G) qRT-PCR analysis confirming overexpression of *zfhx4* in CRISPR-mediated
1051 *betaPix* F_0 knockout embryos with *zfhx4* mRNA injection at 70% epiboly.

1052 (H) Representative stereomicroscopy images of erythrocytes stained with *o*-
1053 dianisidine showing that brain hemorrhages decreased in *bbh*^{fn40a} mutants with
1054 zfhx4 mRNA injection at 48 hpf. Arrows indicate brain hemorrhages. Lateral
1055 views with anterior to the left.

1056 (I) Quantification of hemorrhagic parameters in (H). Left panel showing

1057 hemorrhage percentages with each dot representing an individual experiment

1058 (n>100 each), and right panel showing hemorrhage area with each dot

1059 representing one embryo.

References

1. Sheth, K.N. (2022). Spontaneous Intracerebral Hemorrhage. New England Journal of Medicine *387*, 1589-1596. doi:10.1056/NEJMra2201449.
2. Chiang, P.T., Tsai, L.K., and Tsai, H.H. (2025). New targets in spontaneous intracerebral hemorrhage. Curr Opin Neurol 38, 10-17. 10.1097/wco.0000000000001325.
3. Thangameeran, S.I.M., Pang, C.Y., Lee, C.H., Tsai, S.T., Hu, W.F., and Liew, H.K. (2023). Experimental animal models and evaluation techniques in intracerebral hemorrhage. Tzu Chi Med J *35*, 1-10. 10.4103/tcmj.tcmj_119_22.
4. Isogai, S., Horiguchi, M., and Weinstein, B.M. (2001). The vascular anatomy of the developing zebrafish: an atlas of embryonic and early larval development. Dev Biol *230*, 278-301. 10.1006/dbio.2000.9995.
5. Buchner, D.A., Su, F., Yamaoka, J.S., Kamei, M., Shavit, J.A., Barthel, L.K., McGee, B., Amigo, J.D., Kim, S., Hanosh, A.W., et al. (2007). pak2a mutations cause cerebral hemorrhage in redhead zebrafish. Proceedings of the National Academy of Sciences *104*, 13996-14001. 10.1073/pnas.0700947104.
6. Jin, S.W., Herzog, W., Santoro, M.M., Mitchell, T.S., Frantsve, J., Jungblut, B., Beis, D., Scott, I.C., D'Amico, L.A., Ober, E.A., et al. (2007). A transgene-assisted genetic screen identifies essential regulators of vascular development in vertebrate embryos. Dev Biol 307, 29-42. 10.1016/j.ydbio.2007.03.526.

1082 7. Hegarty, J.M., Yang, H., and Chi, N.C. (2013). UBIAD1-mediated vitamin K2
1083 synthesis is required for vascular endothelial cell survival and development.
1084 Development *140*, 1713-1719. 10.1242/dev.093112.
1085 8. Stainier, D.Y., Fouquet, B., Chen, J.N., Warren, K.S., Weinstein, B.M., Meiler,
1086 S.E., Mohideen, M.A., Neuhauss, S.C., Solnica-Krezel, L., Schier, A.F., et al.
1087 (1996). Mutations affecting the formation and function of the cardiovascular
1088 system in the zebrafish embryo. Development *123*, 285-292.
1089 9. Chen, J.N., van Bebber, F., Goldstein, A.M., Serluca, F.C., Jackson, D., Childs,
1090 S., Serbedzija, G., Warren, K.S., Mably, J.D., Lindahl, P., et al. (2001). Genetic
1091 steps to organ laterality in zebrafish. Comp Funct Genomics *2*, 60-68.
1092 10.1002/cfg.74.
1093 10. Liu, J., Fraser, S.D., Faloon, P.W., Rollins, E.L., Vom Berg, J., Starovic-
1094 Subota, O., Laliberte, A.L., Chen, J.N., Serluca, F.C., and Childs, S.J. (2007).
1095 A betaPix Pak2a signaling pathway regulates cerebral vascular stability in
1096 zebrafish. Proc Natl Acad Sci U S A 104, 13990-13995.
1097 10.1073/pnas.0700825104.
1098 11. Manser, E., Loo, T.H., Koh, C.G., Zhao, Z.S., Chen, X.Q., Tan, L., Tan, I.,
1099 Leung, T., and Lim, L. (1998). PAK kinases are directly coupled to the PIX
1100 family of nucleotide exchange factors. Mol Cell 1, 183-192. 10.1016/s1097-
1101 2765(00)80019-2
1102 12. Zhou, W., Li, X., and Premont, R.T. (2016). Expanding functions of GIT Arf
1103 GTPase-activating proteins, PIX Rho guanine nucleotide exchange factors and

1104 GIT-PIX complexes. J Cell Sci *129*, 1963-1974. 10.1242/jcs.179465.

1105 13. Morimoto, K., Tabata, H., Takahashi, R., and Nakajima, K. (2024).
1106 Interactions between neural cells and blood vessels in central nervous system
1107 development. Bioessays *46*, e2300091. 10.1002/bies.202300091.

1108 14. Grinchevskaya, L.R., Salikhova, D.I., Silachev, D.N., and Goldshtein, D.V.
1109 (2024). Neural and Glial Regulation of Angiogenesis in CNS in Ischemic
1110 Stroke. Bull Exp Biol Med *177*, 528-533. 10.1007/s10517-024-06219-4.

1111 15. McCarty, J.H. (2009). Cell adhesion and signaling networks in brain
1112 neurovascular units. Curr Opin Hematol *16*, 209-214.
1113 10.1097/MOH.0b013e32832a07eb.

1114 16. McCarty, J.H. (2009). Integrin-mediated regulation of neurovascular
1115 development, physiology and disease. Cell Adh Migr *3*, 211-215.
1116 10.4161/cam.3.2.7767.

1117 17. Liu, J., Zeng, L., Kennedy, R.M., Gruenig, N.M., and Childs, S.J. (2012). β
1118 Pix plays a dual role in cerebral vascular stability and angiogenesis, and
1119 interacts with integrin αvβ8. Dev Biol *363*, 95-105.
1120 10.1016/j.ydbio.2011.12.022.

1121 18. Yang, R., Zhang, Y., Huang, D., Luo, X., Zhang, L., Zhu, X., Zhang, X., Liu,
1122 Z., Han, J.Y., and Xiong, J.W. (2017). Miconazole protects blood vessels from
1123 MMP9-dependent rupture and hemorrhage. Dis Model Mech *10*, 337-348.
1124 10.1242/dmm.027268.

1125 19. Sugimoto, K., Hui, S.P., Sheng, D.Z., and Kikuchi, K. (2017). Dissection of

1126 zebrafish shha function using site-specific targeting with a Cre-dependent
1127 genetic switch. Elife *6*. 10.7554/eLife.24635.
1128 20. Ogawa, M., Geng, F.S., Humphreys, D.T., Kristianto, E., Sheng, D.Z., Hui,
1129 S.P., Zhang, Y., Sugimoto, K., Nakayama, M., Zheng, D., et al. (2021). Krü
1130 ppel-like factor 1 is a core cardiomyogenic trigger in zebrafish. Science *372*,
1131 201-205. 10.1126/science.abe2762.
1132 21. Ogawa, M., and Kikuchi, K. (2024). Generation of Conditional Knockout
1133 Zebrafish Using an Invertible Gene-Trap Cassette. Methods Mol Biol *2707*,
1134 205-214. 10.1007/978-1-0716-3401-1_13.
1135 22. Wierson, W.A., Simone, B.W., WareJoncas, Z., Mann, C., Welker, J.M., Kar,
1136 B., Emch, M.J., Friedberg, I., Gendron, W.A.C., Barry, M.A., et al. (2019).
1137 Expanding the CRISPR Toolbox with ErCas12a in Zebrafish and Human
1138 Cells. Crispr j *2*, 417-433. 10.1089/crispr.2019.0026.
1139 23. Wu, R.S., Lam, II, Clay, H., Duong, D.N., Deo, R.C., and Coughlin, S.R.
1140 (2018). A Rapid Method for Directed Gene Knockout for Screening in G0
1141 Zebrafish. Dev Cell *46*, 112-125 e114. 10.1016/j.devcel.2018.06.003.
1142 24. Quiñonez-Silvero, C., Hübner, K., and Herzog, W. (2020). Development of the
1143 brain vasculature and the blood-brain barrier in zebrafish. Dev Biol *457*, 181-
1144 190. 10.1016/j.ydbio.2019.03.005.
1145 25. Deacon, S.W., Beeser, A., Fukui, J.A., Rennefahrt, U.E., Myers, C., Chernoff,
1146 J., and Peterson, J.R. (2008). An isoform-selective, small-molecule inhibitor
1147 targets the autoregulatory mechanism of p21-activated kinase. Chem Biol *15*,

1148 322-331. 10.1016/j.chembiol.2008.03.005.

1149 26. Bernardos, R.L., and Raymond, P.A. (2006). GFAP transgenic zebrafish. Gene
1150 Expr Patterns *6*, 1007-1013. 10.1016/j.modgep.2006.04.006.

1151 27. Kim, C.H., Ueshima, E., Muraoka, O., Tanaka, H., Yeo, S.Y., Huh, T.L., and
1152 Miki, N. (1996). Zebrafish elav/HuC homologue as a very early neuronal
1153 marker. Neurosci Lett *216*, 109-112. 10.1016/0304-3940(96)13021-4.

1154 28. Raj, B., Wagner, D.E., McKenna, A., Pandey, S., Klein, A.M., Shendure, J.,
1155 Gagnon, J.A., and Schier, A.F. (2018). Simultaneous single-cell profiling of
1156 lineages and cell types in the vertebrate brain. Nature Biotechnology *36*, 442-
1157 450. 10.1038/nbt.4103.

1158 29. Raj, B., Farrell, J.A., Liu, J., El Kholtei, J., Carte, A.N., Navajas Acedo, J., Du,
1159 L.Y., McKenna, A., Relić, Đ., Leslie, J.M., and Schier, A.F. (2020).
1160 Emergence of Neuronal Diversity during Vertebrate Brain Development.
1161 Neuron *108*, 1058-1074.e1056. 10.1016/j.neuron.2020.09.023.

1162 30. Farnsworth, D.R., Saunders, L.M., and Miller, A.C. (2020). A single-cell
1163 transcriptome atlas for zebrafish development. Dev Biol 459, 100-108.
1164 10.1016/j.ydbio.2019.11.008.

1165 31. Etienne-Manneville, S. (2013). Microtubules in cell migration. Annu Rev Cell
1166 Dev Biol *29*, 471-499. 10.1146/annurev-cellbio-101011-155711.

1167 32. Kwon, Y., Jeon, Y.W., Kwon, M., Cho, Y., Park, D., and Shin, J.E. (2020). β
1168 Pix-d promotes tubulin acetylation and neurite outgrowth through a
1169 PAK/Stathmin1 signaling pathway. PLoS One *15*, e0230814.

1170 10.1371/journal.pone.0230814.

1171 33. Omelchenko, T., Rabadan, M.A., Hernandez-Martinez, R., Grego-Bessa, J.,
1172 Anderson, K.V., and Hall, A. (2014). beta-Pix directs collective migration of
1173 anterior visceral endoderm cells in the early mouse embryo. Genes Dev *28*,
1174 2764-2777. 10.1101/gad.251371.114.

1175 34. Hsu, R.M., Hsieh, Y.J., Yang, T.H., Chiang, Y.C., Kan, C.Y., Lin, Y.T., Chen,
1176 J.T., and Yu, J.S. (2014). Binding of the extreme carboxyl-terminus of PAK-
1177 interacting exchange factor β (βPIX) to myosin 18A (MYO18A) is required
1178 for epithelial cell migration. Biochim Biophys Acta *1843*, 2513-2527.
1179 10.1016/j.bbamcr.2014.06.023.

1180 35. López Tobón, A., Suresh, M., Jin, J., Vitriolo, A., Pietralla, T., Tedford, K.,
1181 Bossenz, M., Mahnken, K., Kiefer, F., Testa, G., et al. (2018). The guanine
1182 nucleotide exchange factor Arhgef7/βPix promotes axon formation upstream
1183 of TC10. Scientific Reports *8*, 8811. 10.1038/s41598-018-27081-1.

1184 36. Cheng, K., Chahdi, A., Larabee, S.M., Tolaymat, M., Sundel, M.H.,
1185 Drachenberg, C.B., Zhan, M., Hu, S., Said, A.H., Shang, A.C., et al. (2023).
1186 Muscarinic receptor agonist-induced βPix binding to β-catenin promotes
1187 colon neoplasia. Sci Rep *13*, 16920. 10.1038/s41598-023-44158-8.

1188 37. Connor, K., Murray, D.W., Jarzabek, M.A., Tran, N.L., White, K., Dicker, P.,
1189 Sweeney, K.J., O'Halloran, P.J., MacCarthy, B., Shiels, L.P., et al. (2020).
1190 Targeting the RhoGEF βPIX/COOL-1 in Glioblastoma: Proof of Concept
1191 Studies. Cancers (Basel) *12*. 10.3390/cancers12123531.

1192 38. Ward, J.D., Ha, J.H., Jayaraman, M., and Dhanasekaran, D.N. (2015). LPA-
1193 mediated migration of ovarian cancer cells involves translocalization of Gαi2
1194 to invadopodia and association with Src and β-pix. Cancer Lett *356*, 382-391.
1195 10.1016/j.canlet.2014.09.030.
1196 39. Bussmann, J., Wolfe, S.A., and Siekmann, A.F. (2011). Arterial-venous
1197 network formation during brain vascularization involves hemodynamic
1198 regulation of chemokine signaling. Development *138*, 1717-1726.
1199 10.1242/dev.059881.
1200 40. Eubelen, M., Bostaille, N., Cabochette, P., Gauquier, A., Tebabi, P., Dumitru,
1201 A.C., Koehler, M., Gut, P., Alsteens, D., Stainier, D.Y.R., et al. (2018). A
1202 molecular mechanism for Wnt ligand-specific signaling. Science *361*.
1203 10.1126/science.aat1178.
1204 41. Pitulescu, M.E., and Adams, R.H. (2014). Regulation of signaling interactions
1205 and receptor endocytosis in growing blood vessels. Cell Adh Migr *8*, 366-377.
1206 10.4161/19336918.2014.970010.
1207 42. Wang, J., Chen, Y., Zeng, Z., Feng, R., Wang, Q., Zhang, Q., Sun, K., Chen,
1208 A.F., Lu, Y., and Yu, Y. (2021). HMGA2 contributes to vascular development
1209 and sprouting angiogenesis by promoting IGFBP2 production. Exp Cell Res
1210 *408*, 112831. 10.1016/j.yexcr.2021.112831.
1211 43. Fu, C., An, N., Liu, J., A, J., Zhang, B., Liu, M., Zhang, Z., Fu, L., Tian, X.,
1212 Wang, D., and Dong, J.T. (2020). The transcription factor ZFHX3 is crucial
1213 for the angiogenic function of hypoxia-inducible factor 1α in liver cancer

1214 cells. J Biol Chem *295*, 7060-7074. 10.1074/jbc.RA119.012131.

1215 44. Gudbjartsson, D.F., Holm, H., Gretarsdottir, S., Thorleifsson, G., Walters,
1216 G.B., Thorgeirsson, G., Gulcher, J., Mathiesen, E.B., Njølstad, I., Nyrnes, A.,
1217 et al. (2009). A sequence variant in ZFHX3 on 16q22 associates with atrial
1218 fibrillation and ischemic stroke. Nat Genet *41*, 876-878. 10.1038/ng.417.

1219 45. Soriano-Tárraga, C., Lazcano, U., Giralt-Steinhauer, E., Avellaneda-Gómez,
1220 C., Ois, Á., Rodríguez-Campello, A., Cuadrado-Godia, E., Gómez-González,
1221 A., Fernández-Sanlés, A., Elosua, R., et al. (2020). Identification of 20 novel
1222 loci associated with ischaemic stroke. Epigenome-wide association study.
1223 Epigenetics *15*, 988-997. 10.1080/15592294.2020.1746507.

1224 46. Malik, R., Traylor, M., Pulit, S.L., Bevan, S., Hopewell, J.C., Holliday, E.G.,
1225 Zhao, W., Abrantes, P., Amouyel, P., Attia, J.R., et al. (2016). Low-frequency
1226 and common genetic variation in ischemic stroke: The METASTROKE
1227 collaboration. Neurology *86*, 1217-1226. 10.1212/wnl.0000000000002528.

1228 47. Kalvaitytė, M., and Balciunas, D. (2022). Conditional mutagenesis strategies
1229 in zebrafish. Trends Genet *38*, 856-868. 10.1016/j.tig.2022.04.007.

1230 48. Obermeier, B., Daneman, R., and Ransohoff, R.M. (2013). Development,
1231 maintenance and disruption of the blood-brain barrier. Nat Med *19*, 1584-
1232 1596. 10.1038/nm.3407.

1233 49. Langen, U.H., Ayloo, S., and Gu, C. (2019). Development and Cell Biology of
1234 the Blood-Brain Barrier. Annu Rev Cell Dev Biol *35*, 591-613.
1235 10.1146/annurev-cellbio-100617-062608.

1236 50. Fleming, A., Diekmann, H., and Goldsmith, P. (2013). Functional
1237 characterisation of the maturation of the blood-brain barrier in larval zebrafish.
1238 PLoS One *8*, e77548. 10.1371/journal.pone.0077548.
1239 51. Xie, J., Farage, E., Sugimoto, M., and Anand-Apte, B. (2010). A novel
1240 transgenic zebrafish model for blood-brain and blood-retinal barrier
1241 development. BMC Dev Biol *10*, 76. 10.1186/1471-213x-10-76.
1242 52. Armulik, A., Genove, G., and Betsholtz, C. (2011). Pericytes: developmental,
1243 physiological, and pathological perspectives, problems, and promises. Dev
1244 Cell *21*, 193-215. 10.1016/j.devcel.2011.07.001.
1245 53. Armulik, A., Genové, G., Mäe, M., Nisancioglu, M.H., Wallgard, E., Niaudet,
1246 C., He, L., Norlin, J., Lindblom, P., Strittmatter, K., et al. (2010). Pericytes
1247 regulate the blood-brain barrier. Nature *468*, 557-561. 10.1038/nature09522.
1248 54. Bell, R.D., Winkler, E.A., Sagare, A.P., Singh, I., LaRue, B., Deane, R., and
1249 Zlokovic, B.V. (2010). Pericytes control key neurovascular functions and
1250 neuronal phenotype in the adult brain and during brain aging. Neuron *68*, 409-
1251 427. 10.1016/j.neuron.2010.09.043.
1252 55. Daneman, R., Zhou, L., Kebede, A.A., and Barres, B.A. (2010). Pericytes are
1253 required for blood-brain barrier integrity during embryogenesis. Nature *468*,
1254 562-566. 10.1038/nature09513.
1255 56. Antonelli-Orlidge, A., Saunders, K.B., Smith, S.R., and D'Amore, P.A. (1989).
1256 An activated form of transforming growth factor beta is produced by
1257 cocultures of endothelial cells and pericytes. Proc Natl Acad Sci U S A *86*,

1258 4544-4548. 10.1073/pnas.86.12.4544.

1259 57. Dohgu, S., Takata, F., Yamauchi, A., Nakagawa, S., Egawa, T., Naito, M.,
1260 Tsuruo, T., Sawada, Y., Niwa, M., and Kataoka, Y. (2005). Brain pericytes
1261 contribute to the induction and up-regulation of blood-brain barrier functions
1262 through transforming growth factor-beta production. Brain Res *1038*, 208-215.
1263 10.1016/j.brainres.2005.01.027.

1264 58. Dave, J.M., Mirabella, T., Weatherbee, S.D., and Greif, D.M. (2018). Pericyte
1265 ALK5/TIMP3 Axis Contributes to Endothelial Morphogenesis in the
1266 Developing Brain. Dev Cell *44*, 665-678.e666. 10.1016/j.devcel.2018.01.018.

1267 59. Reyahi, A., Nik, A.M., Ghiami, M., Gritli-Linde, A., Pontén, F., Johansson,
1268 B.R., and Carlsson, P. (2015). Foxf2 Is Required for Brain Pericyte
1269 Differentiation and Development and Maintenance of the Blood-Brain Barrier.
1270 Dev Cell *34*, 19-32. 10.1016/j.devcel.2015.05.008.

1271 60. Kim, Y., Imdad, R.Y., Stephenson, A.H., Sprague, R.S., and Lonigro, A.J.
1272 (1998). Vascular endothelial growth factor mRNA in pericytes is upregulated
1273 by phorbol myristate acetate. Hypertension *31*, 511-515.
1274 10.1161/01.hyp.31.1.511.

1275 61. Franco, M., Roswall, P., Cortez, E., Hanahan, D., and Pietras, K. (2011).
1276 Pericytes promote endothelial cell survival through induction of autocrine
1277 VEGF-A signaling and Bcl-w expression. Blood *118*, 2906-2917.
1278 10.1182/blood-2011-01-331694.

1279 62. Sato, T.N., Tozawa, Y., Deutsch, U., Wolburg-Buchholz, K., Fujiwara, Y.,

1280 Gendron-Maguire, M., Gridley, T., Wolburg, H., Risau, W., and Qin, Y. (1995).
1281 Distinct roles of the receptor tyrosine kinases Tie-1 and Tie-2 in blood vessel
1282 formation. Nature *376*, 70-74. 10.1038/376070a0.
1283 63. Thurston, G., Suri, C., Smith, K., McClain, J., Sato, T.N., Yancopoulos, G.D.,
1284 and McDonald, D.M. (1999). Leakage-resistant blood vessels in mice
1285 transgenically overexpressing angiopoietin-1. Science *286*, 2511-2514.
1286 10.1126/science.286.5449.2511.
1287 64. Sundberg, C., Kowanetz, M., Brown, L.F., Detmar, M., and Dvorak, H.F.
1288 (2002). Stable expression of angiopoietin-1 and other markers by cultured
1289 pericytes: phenotypic similarities to a subpopulation of cells in maturing
1290 vessels during later stages of angiogenesis in vivo. Lab Invest *82*, 387-401.
1291 10.1038/labinvest.3780433.
1292 65. Wan, Y., Jin, H.J., Zhu, Y.Y., Fang, Z., Mao, L., He, Q., Xia, Y.P., Li, M., Li,
1293 Y., Chen, X., and Hu, B. (2018). MicroRNA-149-5p regulates blood-brain
1294 barrier permeability after transient middle cerebral artery occlusion in rats by
1295 targeting S1PR2 of pericytes. Faseb j *32*, 3133-3148. 10.1096/fj.201701121R.
1296 66. Li, F., Lan, Y., Wang, Y., Wang, J., Yang, G., Meng, F., Han, H., Meng, A.,
1297 Wang, Y., and Yang, X. (2011). Endothelial Smad4 maintains cerebrovascular
1298 integrity by activating N-cadherin through cooperation with Notch. Dev Cell
1299 *20*, 291-302. 10.1016/j.devcel.2011.01.011.
1300 67. Liu, H., Zhang, W., Kennard, S., Caldwell, R.B., and Lilly, B. (2010). Notch3
1301 is critical for proper angiogenesis and mural cell investment. Circ Res *107*,

1302 860-870. 10.1161/circresaha.110.218271.

1303 68. Gundersen, G.A., Vindedal, G.F., Skare, O., and Nagelhus, E.A. (2014).
1304 Evidence that pericytes regulate aquaporin-4 polarization in mouse cortical
1305 astrocytes. Brain Struct Funct *219*, 2181-2186. 10.1007/s00429-013-0629-0.

1306 69. Jeanne, M., Jorgensen, J., and Gould, D.B. (2015). Molecular and Genetic
1307 Analyses of Collagen Type IV Mutant Mouse Models of Spontaneous
1308 Intracerebral Hemorrhage Identify Mechanisms for Stroke Prevention.
1309 Circulation *131*, 1555-1565. 10.1161/circulationaha.114.013395.

1310 70. Gautam, J., Zhang, X., and Yao, Y. (2016). The role of pericytic laminin in
1311 blood brain barrier integrity maintenance. Sci Rep *6*, 36450.
1312 10.1038/srep36450.

1313 71. Gautam, J., Cao, Y., and Yao, Y. (2020). Pericytic Laminin Maintains Blood-
1314 Brain Barrier Integrity in an Age-Dependent Manner. Transl Stroke Res *11*,
1315 228-242. 10.1007/s12975-019-00709-8.

1316 72. Özkan, E., Çetin-Taş, Y., Şekerdağ, E., Kızılırmak, A.B., Taş, A., Yıldız, E.,
1317 Yapıcı-Eser, H., Karahüseyinoğlu, S., Zeybel, M., and Gürsoy-Özdemir, Y.
1318 (2021). Blood-brain barrier leakage and perivascular collagen accumulation
1319 precede microvessel rarefaction and memory impairment in a chronic
1320 hypertension animal model. Metab Brain Dis *36*, 2553-2566. 10.1007/s11011-
1321 021-00767-8.

1322 73. Stewart, P.A., and Wiley, M.J. (1981). Developing nervous tissue induces
1323 formation of blood-brain barrier characteristics in invading endothelial cells: a

study using quail--chick transplantation chimeras. Dev Biol *84*, 183-192. 10.1016/0012-1606(81)90382-1.

74. Hellström, M., Kalén, M., Lindahl, P., Abramsson, A., and Betsholtz, C. (1999). Role of PDGF-B and PDGFR-beta in recruitment of vascular smooth muscle cells and pericytes during embryonic blood vessel formation in the mouse. Development *126*, 3047-3055.

75. Bjarnegård, M., Enge, M., Norlin, J., Gustafsdottir, S., Fredriksson, S., Abramsson, A., Takemoto, M., Gustafsson, E., Fässler, R., and Betsholtz, C. (2004). Endothelium-specific ablation of PDGFB leads to pericyte loss and glomerular, cardiac and placental abnormalities. Development *131*, 1847-1857. 10.1242/dev.01080.

76. Mi, H., Haeberle, H., and Barres, B.A. (2001). Induction of astrocyte differentiation by endothelial cells. J Neurosci *21*, 1538-1547. 10.1523/jneurosci.21-05-01538.2001.

77. Paredes, I., Vieira, J.R., Shah, B., Ramunno, C.F., Dyckow, J., Adler, H., Richter, M., Schermann, G., Giannakouri, E., Schirmer, L., et al. (2021). Oligodendrocyte precursor cell specification is regulated by bidirectional neural progenitor-endothelial cell crosstalk. Nat Neurosci *24*, 478-488. 10.1038/s41593-020-00788-z.

78. Daneman, R., Agalliu, D., Zhou, L., Kuhnert, F., Kuo, C.J., and Barres, B.A. (2009). Wnt/beta-catenin signaling is required for CNS, but not non-CNS, angiogenesis. Proc Natl Acad Sci U S A *106*, 641-646.

1346 10.1073/pnas.0805165106.

1347 79. Kuhnert, F., Mancuso, M.R., Shamloo, A., Wang, H.T., Choksi, V., Florek, M.,
1348 Su, H., Fruttiger, M., Young, W.L., Heilshorn, S.C., and Kuo, C.J. (2010).
1349 Essential regulation of CNS angiogenesis by the orphan G protein-coupled
1350 receptor GPR124. Science *330*, 985-989. 10.1126/science.1196554.

1351 80. Cullen, M., Elzarrad, M.K., Seaman, S., Zudaire, E., Stevens, J., Yang, M.Y.,
1352 Li, X., Chaudhary, A., Xu, L., Hilton, M.B., et al. (2011). GPR124, an orphan
1353 G protein-coupled receptor, is required for CNS-specific vascularization and
1354 establishment of the blood-brain barrier. Proc Natl Acad Sci U S A *108*, 5759-
1355 5764. 10.1073/pnas.1017192108.

1356 81. Zhou, Y., and Nathans, J. (2014). Gpr124 controls CNS angiogenesis and
1357 blood-brain barrier integrity by promoting ligand-specific canonical wnt
1358 signaling. Dev Cell *31*, 248-256. 10.1016/j.devcel.2014.08.018.

1359 82. Thomas, M., and Augustin, H.G. (2009). The role of the Angiopoietins in
1360 vascular morphogenesis. Angiogenesis *12*, 125-137. 10.1007/s10456-009-
1361 9147-3.

1362 83. Nico, B., Frigeri, A., Nicchia, G.P., Quondamatteo, F., Herken, R., Errede, M.,
1363 Ribatti, D., Svelto, M., and Roncali, L. (2001). Role of aquaporin-4 water
1364 channel in the development and integrity of the blood-brain barrier. J Cell Sci
1365 *114*, 1297-1307. 10.1242/jcs.114.7.1297.

1366 84. Nicchia, G.P., Nico, B., Camassa, L.M., Mola, M.G., Loh, N., Dermietzel, R.,
1367 Spray, D.C., Svelto, M., and Frigeri, A. (2004). The role of aquaporin-4 in the

1368 blood-brain barrier development and integrity: studies in animal and cell
1369 culture models. Neuroscience *129*, 935-945.
1370 10.1016/j.neuroscience.2004.07.055.
1371 85. Hartfuss, E., Galli, R., Heins, N., and Götz, M. (2001). Characterization of
1372 CNS precursor subtypes and radial glia. Dev Biol *229*, 15-30.
1373 10.1006/dbio.2000.9962.
1374 86. Malatesta, P., Appolloni, I., and Calzolari, F. (2008). Radial glia and neural
1375 stem cells. Cell Tissue Res *331*, 165-178. 10.1007/s00441-007-0481-8.
1376 87. Qian, X., Shen, Q., Goderie, S.K., He, W., Capela, A., Davis, A.A., and
1377 Temple, S. (2000). Timing of CNS cell generation: a programmed sequence of
1378 neuron and glial cell production from isolated murine cortical stem cells.
1379 Neuron *28*, 69-80. 10.1016/s0896-6273(00)00086-6.
1380 88. Price, J., Williams, B.P., and Götz, M. (1995). The generation of cellular
1381 diversity in the cerebral cortex. Ciba Found Symp *193*, 71-84; discussion 117-
1382 126. 10.1002/9780470514795.ch4.
1383 89. Grupp, L., Wolburg, H., and Mack, A.F. (2010). Astroglial structures in the
1384 zebrafish brain. J Comp Neurol *518*, 4277-4287. 10.1002/cne.22481.
1385 90. Chen, J., Poskanzer, K.E., Freeman, M.R., and Monk, K.R. (2020). Live-
1386 imaging of astrocyte morphogenesis and function in zebrafish neural circuits.
1387 Nat Neurosci *23*, 1297-1306. 10.1038/s41593-020-0703-x.
1388 91. Johnson, K., Barragan, J., Bashiruddin, S., Smith, C.J., Tyrrell, C., Parsons,
1389 M.J., Doris, R., Kucenas, S., Downes, G.B., Velez, C.M., et al. (2016). Gfap-

positive radial glial cells are an essential progenitor population for later-born neurons and glia in the zebrafish spinal cord. Glia *64*, 1170-1189. 10.1002/glia.22990.

92. Umans, R.A., Pollock, C., Mills, W.A., 3rd, Clark, K.C., Pan, Y.A., and Sontheimer, H. (2021). Using Zebrafish to Elucidate Glial-Vascular Interactions During CNS Development. Front Cell Dev Biol *9*, 654338. 10.3389/fcell.2021.654338.

93. Matsuoka, R.L., Rossi, A., Stone, O.A., and Stainier, D.Y.R. (2017). CNS-resident progenitors direct the vascularization of neighboring tissues. Proc Natl Acad Sci U S A *114*, 10137-10142. 10.1073/pnas.1619300114.

94. Alvarez, J.I., Dodelet-Devillers, A., Kebir, H., Ifergan, I., Fabre, P.J., Terouz, S., Sabbagh, M., Wosik, K., Bourbonnière, L., Bernard, M., et al. (2011). The Hedgehog pathway promotes blood-brain barrier integrity and CNS immune quiescence. Science *334*, 1727-1731. 10.1126/science.1206936.

95. Brilha, S., Ong, C.W.M., Weksler, B., Romero, N., Couraud, P.O., and Friedland, J.S. (2017). Matrix metalloproteinase-9 activity and a downregulated Hedgehog pathway impair blood-brain barrier function in an in vitro model of CNS tuberculosis. Sci Rep *7*, 16031. 10.1038/s41598-017-16250-3.

96. Shi, T., Yue, S., Xie, C., Li, X., Yang, D., Hu, L., Zhong, Y., Zhang, Y., and Liu, W. (2024). MMP-2-mediated Scube2 degradation promotes blood-brain barrier disruption by blocking the interaction between astrocytes and

1412 endothelial cells via inhibiting Sonic hedgehog pathway during early cerebral
1413 ischemia. J Neurochem *168*, 1877-1894. 10.1111/jnc.16021.
1414 97. Xing, G., Zhao, T., Zhang, X., Li, H., Li, X., Cui, P., Li, M., Li, D., Zhang, N.,
1415 and Jiang, W. (2020). Astrocytic Sonic Hedgehog Alleviates Intracerebral
1416 Hemorrhagic Brain Injury via Modulation of Blood-Brain Barrier Integrity.
1417 Front Cell Neurosci *14*, 575690. 10.3389/fncel.2020.575690.
1418 98. Lawson, N.D., Vogel, A.M., and Weinstein, B.M. (2002). sonic hedgehog and
1419 vascular endothelial growth factor act upstream of the Notch pathway during
1420 arterial endothelial differentiation. Dev Cell *3*, 127-136. 10.1016/s1534-
1421 5807(02)00198-3.
1422 99. Mannan, A., Dhiamn, S., Garg, N., and Singh, T.G. (2023). Pharmacological
1423 modulation of Sonic Hedgehog signaling pathways in Angiogenesis: A
1424 mechanistic perspective. Dev Biol *504*, 58-74. 10.1016/j.ydbio.2023.09.009.
1425 100. Argaw, A.T., Asp, L., Zhang, J., Navrazhina, K., Pham, T., Mariani, J.N.,
1426 Mahase, S., Dutta, D.J., Seto, J., Kramer, E.G., et al. (2012). Astrocyte-derived
1427 VEGF-A drives blood-brain barrier disruption in CNS inflammatory disease. J
1428 Clin Invest *122*, 2454-2468. 10.1172/jci60842.
1429 101. Chapouly, C., Tadesse Argaw, A., Horng, S., Castro, K., Zhang, J., Asp, L.,
1430 Loo, H., Laitman, B.M., Mariani, J.N., Straus Farber, R., et al. (2015).
1431 Astrocytic TYMP and VEGFA drive blood-brain barrier opening in
1432 inflammatory central nervous system lesions. Brain *138*, 1548-1567.
1433 10.1093/brain/awv077.

1434 102. Matsumoto, T., and Mugishima, H. (2006). Signal transduction via vascular
1435 endothelial growth factor (VEGF) receptors and their roles in atherogenesis. J
1436 Atheroscler Thromb *13*, 130-135. 10.5551/jat.13.130.
1437 103. Jakobsson, L., Franco, C.A., Bentley, K., Collins, R.T., Ponsioen, B., Aspalter,
1438 I.M., Rosewell, I., Busse, M., Thurston, G., Medvinsky, A., et al. (2010).
1439 Endothelial cells dynamically compete for the tip cell position during
1440 angiogenic sprouting. Nature Cell Biology *12*, 943-953. 10.1038/ncb2103.
1441 104. Liu, Z.J., Shirakawa, T., Li, Y., Soma, A., Oka, M., Dotto, G.P., Fairman,
1442 R.M., Velazquez, O.C., and Herlyn, M. (2003). Regulation of Notch1 and Dll4
1443 by vascular endothelial growth factor in arterial endothelial cells: implications
1444 for modulating arteriogenesis and angiogenesis. Mol Cell Biol *23*, 14-25.
1445 10.1128/mcb.23.1.14-25.2003.
1446 105. Olsson, A.K., Dimberg, A., Kreuger, J., and Claesson-Welsh, L. (2006). VEGF
1447 receptor signalling - in control of vascular function. Nat Rev Mol Cell Biol *7*,
1448 359-371. 10.1038/nrm1911.
1449 106. Xu, L., Nirwane, A., and Yao, Y. (2019). Basement membrane and blood-brain
1450 barrier. Stroke Vasc Neurol *4*, 78-82. 10.1136/svn-2018-000198.
1451 107. Halder, S.K., Sapkota, A., and Milner, R. (2022). The impact of genetic
1452 manipulation of laminin and integrins at the blood-brain barrier. Fluids
1453 Barriers CNS *19*, 50. 10.1186/s12987-022-00346-8.
1454 108. Yao, Y., Chen, Z.L., Norris, E.H., and Strickland, S. (2014). Astrocytic laminin
1455 regulates pericyte differentiation and maintains blood brain barrier integrity.

1456 Nat Commun *5*, 3413. 10.1038/ncomms4413.

1457 109. Milner, R., and Campbell, I.L. (2002). Developmental regulation of beta1
1458 integrins during angiogenesis in the central nervous system. Mol Cell
1459 Neurosci *20*, 616-626. 10.1006/mcne.2002.1151.

1460 110. Nishimura, S.L., Boylen, K.P., Einheber, S., Milner, T.A., Ramos, D.M., and
1461 Pytela, R. (1998). Synaptic and glial localization of the integrin alphavbeta8 in
1462 mouse and rat brain. Brain Res *791*, 271-282. 10.1016/s0006-8993(98)00118-
1463 8.

1464 111. McCarty, J.H., Lacy-Hulbert, A., Charest, A., Bronson, R.T., Crowley, D.,
1465 Housman, D., Savill, J., Roes, J., and Hynes, R.O. (2005). Selective ablation
1466 of alphav integrins in the central nervous system leads to cerebral hemorrhage,
1467 seizures, axonal degeneration and premature death. Development *132*, 165-
1468 176. 10.1242/dev.01551.

1469 112. Beis, D., Bartman, T., Jin, S.W., Scott, I.C., D'Amico, L.A., Ober, E.A.,
1470 Verkade, H., Frantsve, J., Field, H.A., Wehman, A., et al. (2005). Genetic and
1471 cellular analyses of zebrafish atrioventricular cushion and valve development.
1472 Development *132*, 4193-4204. 10.1242/dev.01970.

1473 113. Jin, S.W., Beis, D., Mitchell, T., Chen, J.N., and Stainier, D.Y. (2005). Cellular
1474 and molecular analyses of vascular tube and lumen formation in zebrafish.
1475 Development *132*, 5199-5209. 10.1242/dev.02087.

1476 114. Chang, N., Sun, C., Gao, L., Zhu, D., Xu, X., Zhu, X., Xiong, J.W., and Xi,
1477 J.J. (2013). Genome editing with RNA-guided Cas9 nuclease in zebrafish

1478 embryos. Cell Res *23*, 465-472. 10.1038/cr.2013.45.

1479 115. Jao, L.E., Wente, S.R., and Chen, W. (2013). Efficient multiplex biallelic
1480 zebrafish genome editing using a CRISPR nuclease system. Proc Natl Acad
1481 Sci U S A 110, 13904-13909. 10.1073/pnas.1308335110.

1482 116. Kawakami, K. (2004). Transgenesis and gene trap methods in zebrafish by
1483 using the Tol2 transposable element. Methods Cell Biol *77*, 201-222.
1484 10.1016/s0091-679x(04)77011-9.

1485 117. Lei, L., Yan, S.Y., Yang, R., Chen, J.Y., Li, Y., Bu, Y., Chang, N., Zhou, Q.,
1486 Zhu, X., Li, C.Y., and Xiong, J.W. (2017). Spliceosomal protein eftud2
1487 mutation leads to p53-dependent apoptosis in zebrafish neural progenitors.
1488 Nucleic Acids Res *45*, 3422-3436. 10.1093/nar/gkw1043.

1489 118. Pang, M., Bai, L., Zong, W., Wang, X., Bu, Y., Xiong, C., Zheng, J., Li, J.,
1490 Gao, W., Feng, Z., et al. (2020). Light-sheet fluorescence imaging charts the
1491 gastrula origin of vascular endothelial cells in early zebrafish embryos. Cell
1492 Discovery *6*, 74. 10.1038/s41421-020-00204-7.

1493

Figure 1

A

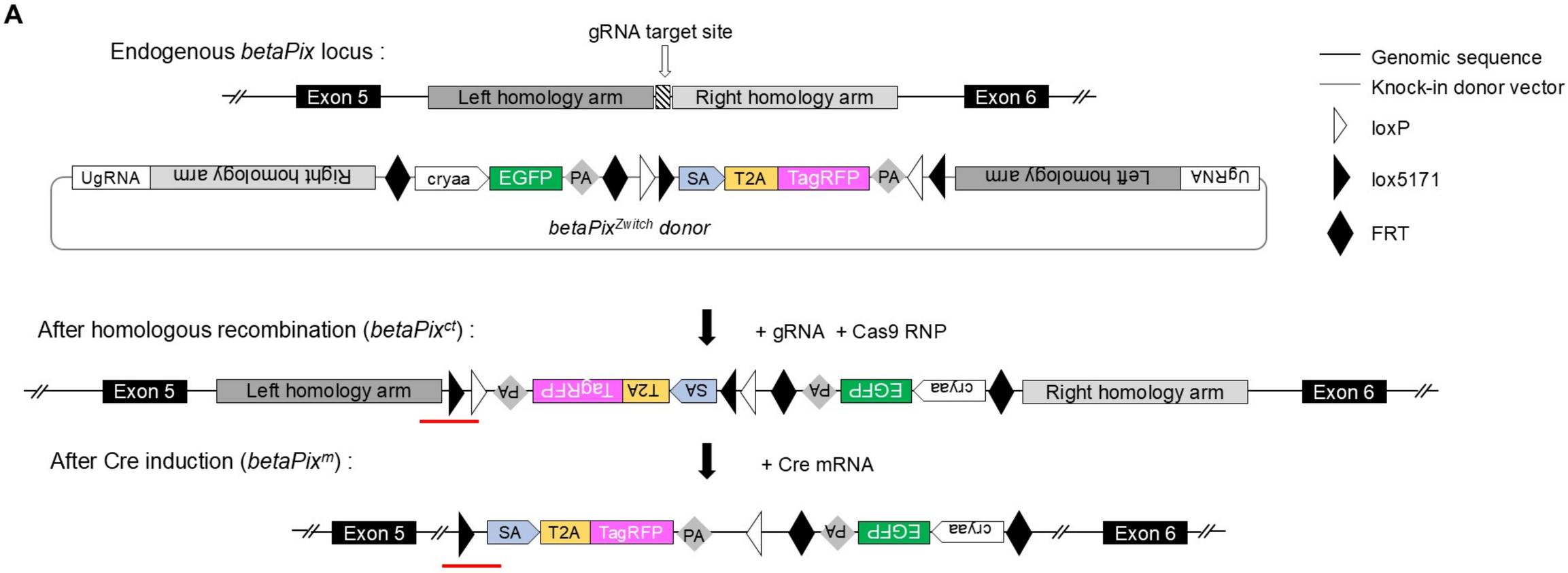

B

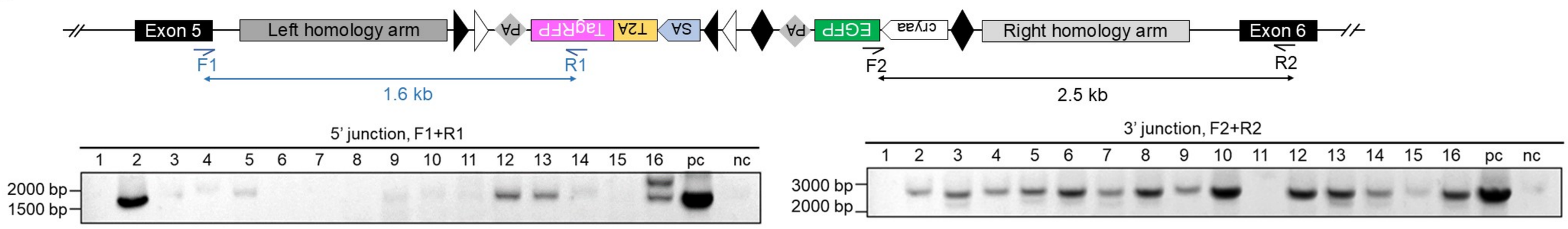

C

D

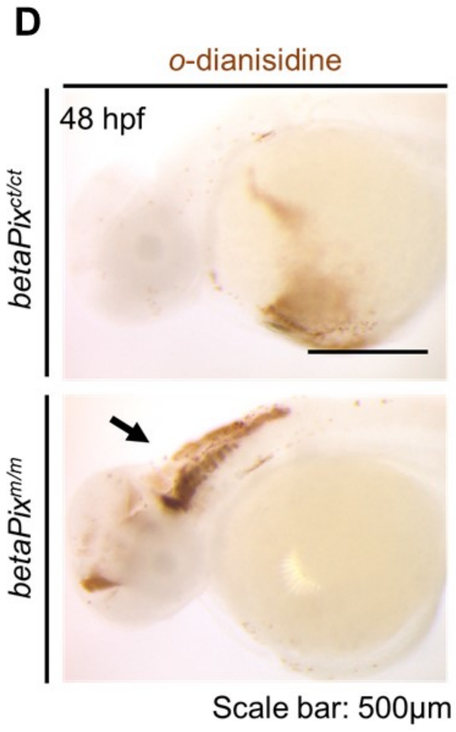

E

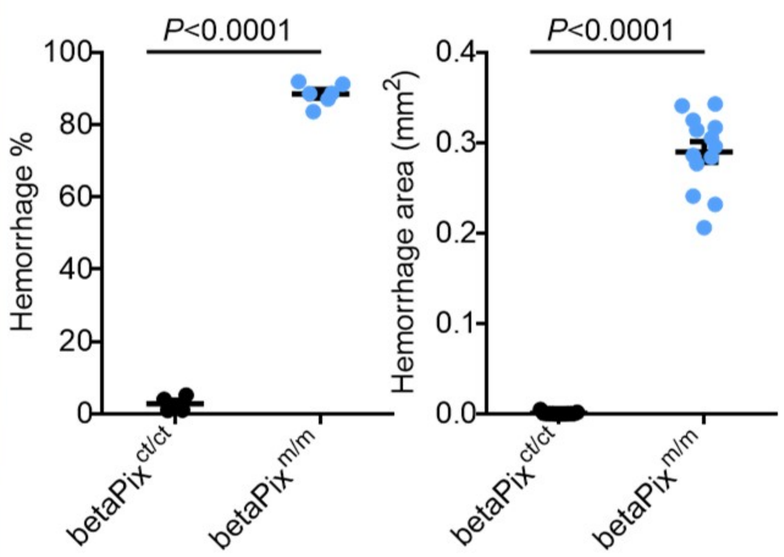

F

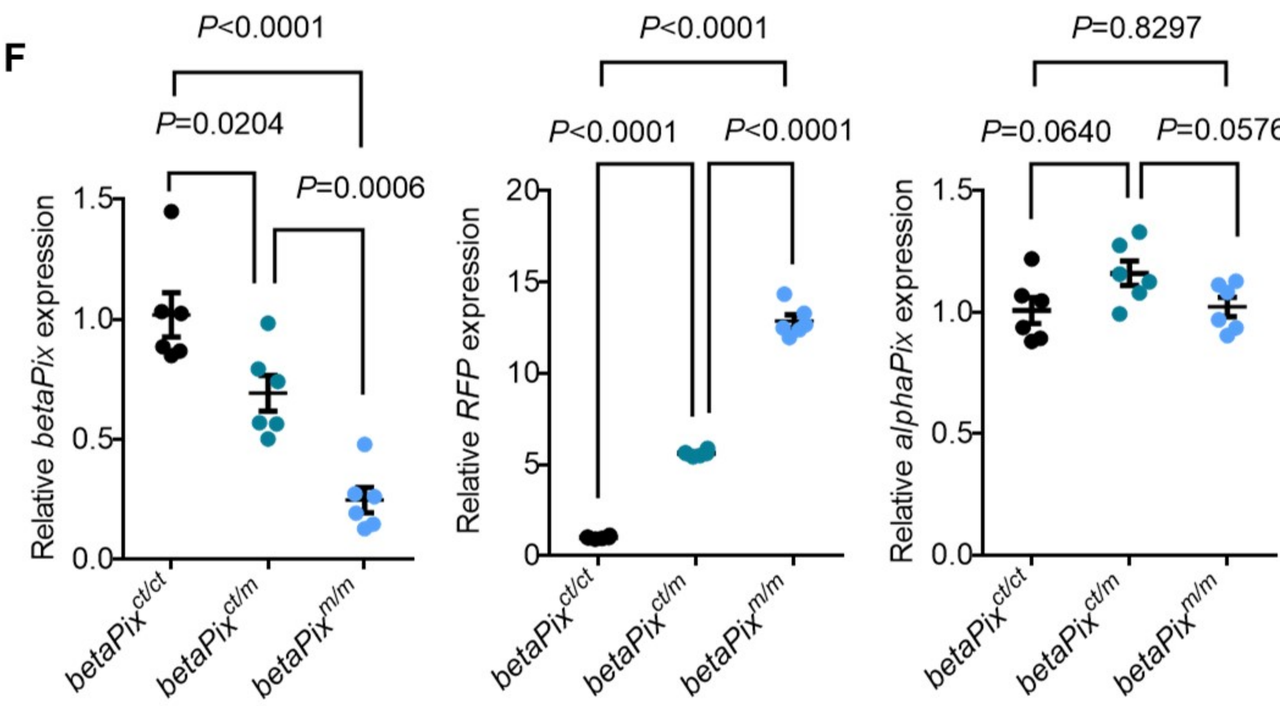

Figure 2

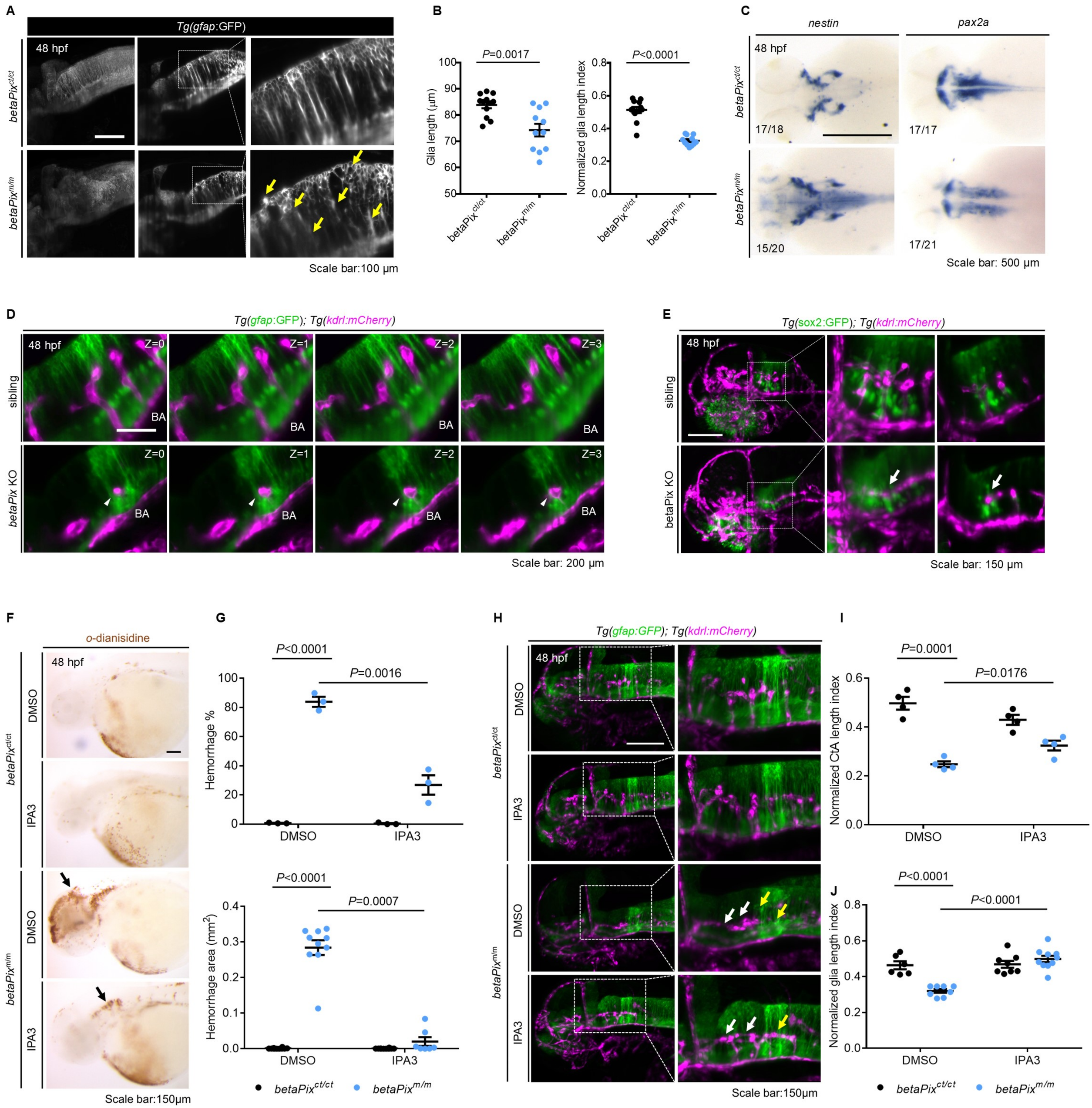
A
Tg(gfap:GFP)
48 hpf
betaPix ct/ct
betaPix m/m
Scale bar:100 µm
B
P=0.0017
P<0.0001
Glia length (µm)
Normalized glia length index
betaPix ct/ct
betaPix m/m
C
nestin
pax2a
48 hpf
17/18
17/17
15/20
17/21
Scale bar: 500 µm
D
Tg(gfap:GFP); Tg(kdrl:mCherry)
sibling
betaPix KO
Z=0
Z=1
Z=2
Z=3
BA
Scale bar: 200 µm
E
Tg(sox2:GFP); Tg(kdrl:mCherry)
48 hpf
sibling
betaPix KO
Scale bar: 150 µm
F
o-dianisidine
48 hpf
DMSO
IPA3
betaPix ct/ct
betaPix m/m
Scale bar:150µm
G
P<0.0001
P=0.0016
Hemorrhage %
P<0.0001
P=0.0007
Hemorrhage area (mm2)
DMSO
IPA3
betaPix ct/ct
betaPix m/m
H
Tg(gfap:GFP); Tg(kdrl:mCherry)
48 hpf
DMSO
IPA3
betaPix ct/ct
betaPix m/m
Scale bar:150µm
I
P=0.0001
P=0.0176
Normalized CtA length index
J
P<0.0001
P<0.0001
Normalized glia length index
DMSO
IPA3
betaPix ct/ct
betaPix m/m

Figure 3

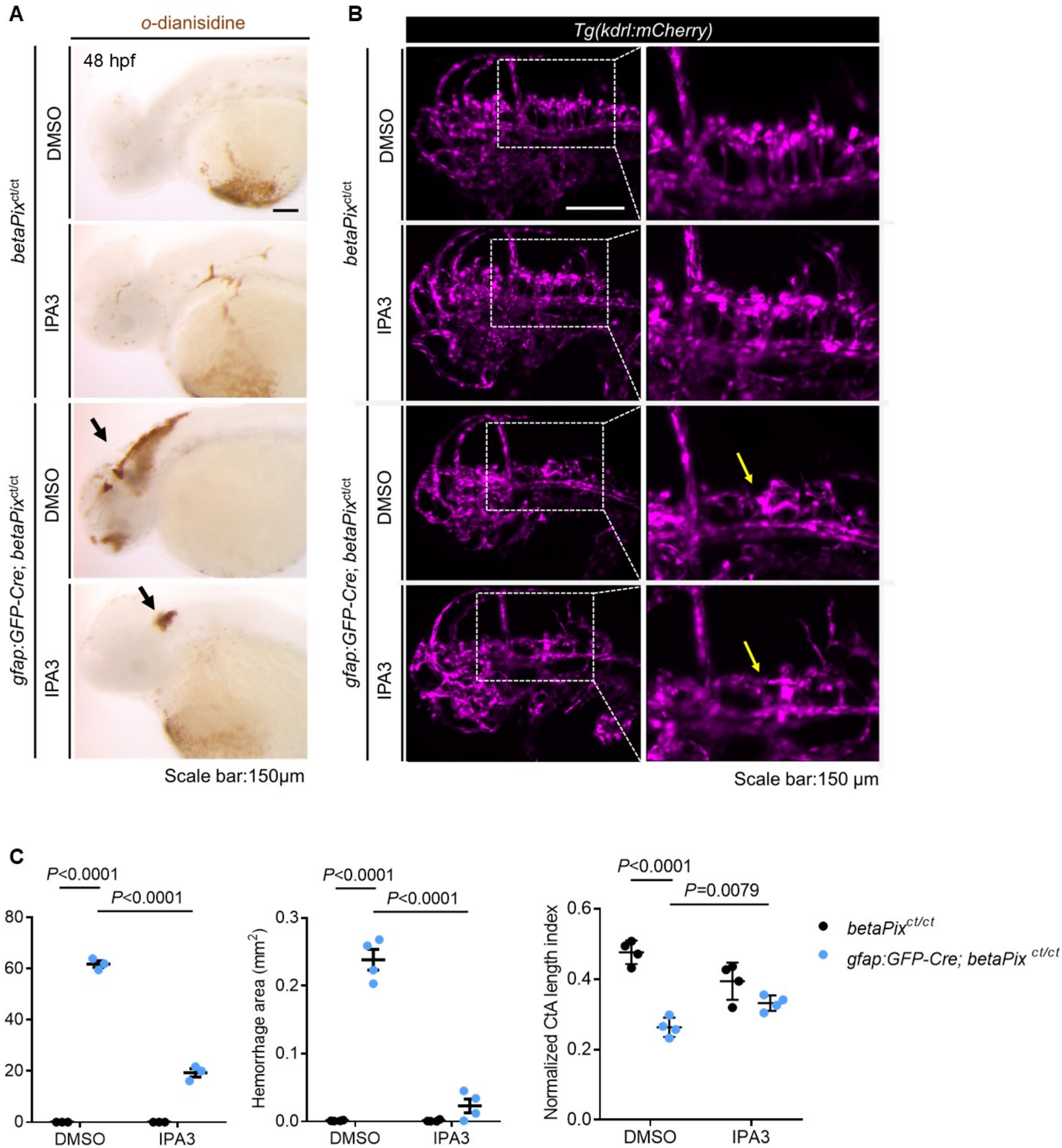
A
o-dianisidine
48 hpf
betaPix ct/ct
gfap:GFP-Cre; betaPix ct/ct
DMSO
IPA3
DMSO
IPA3
Scale bar:150μm
B
Tg(kdrl:mCherry)
betaPix ct/ct
gfap:GFP-Cre; betaPix ct/ct
DMSO
IPA3
DMSO
IPA3
Scale bar:150 μm
C
P<0.0001
P<0.0001
Hemorrhage %
80
60
40
20
0
DMSO
IPA3
P<0.0001
P<0.0001
Hemorrhage area (mm2)
0.3
0.2
0.1
0.0
DMSO
IPA3
P<0.0001
P=0.0079
Normalized CtA length index
0.6
0.4
0.2
0.0
DMSO
IPA3
betaPix ct/ct
gfap:GFP-Cre; betaPix ct/ct

Figure 4

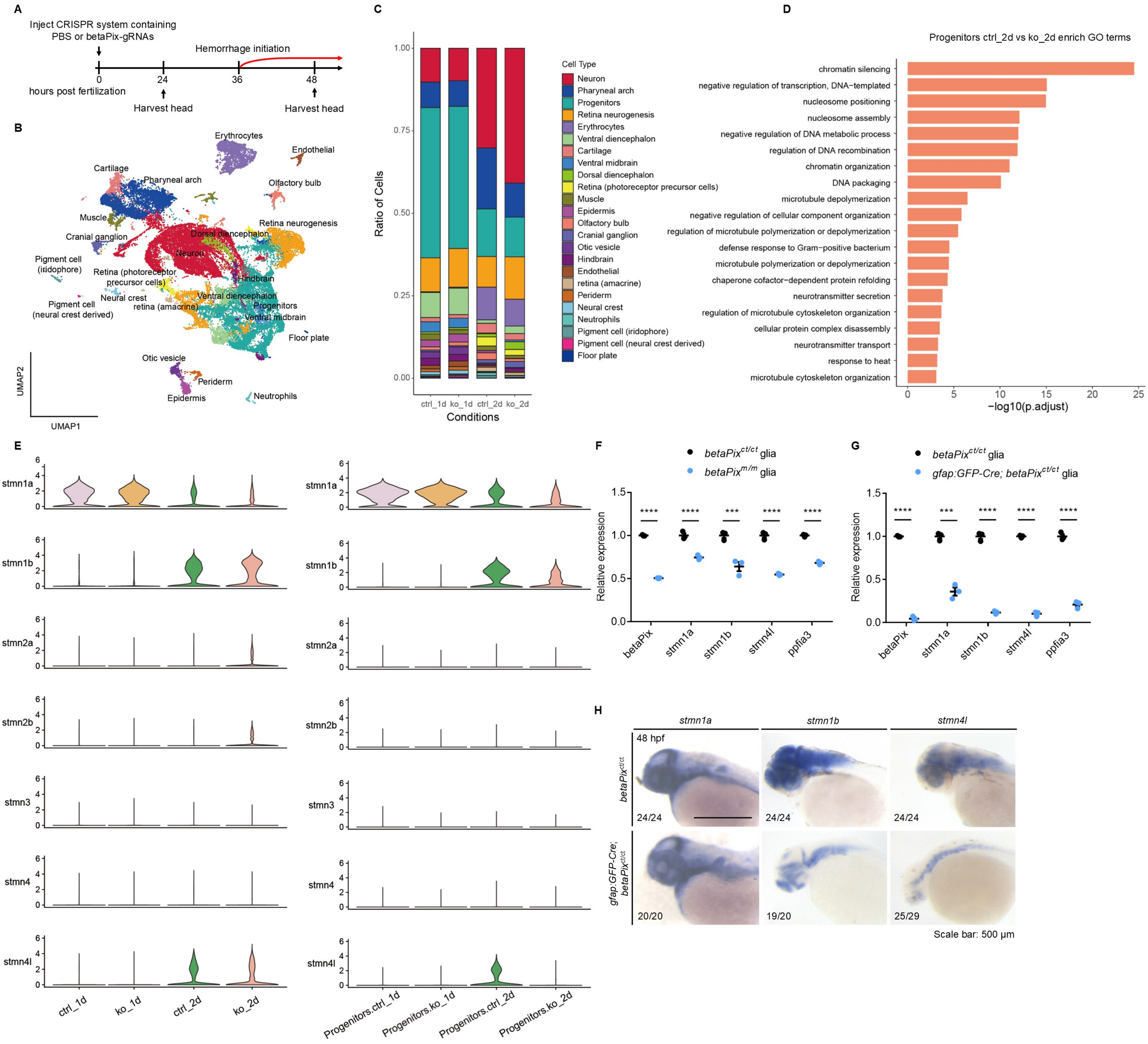
A
Inject CRISPR system containing PBS or betaPix-gRNAs
Hemorrhage initiation
0
24
36
48
hours post fertilization
Harvest head
Harvest head
B
Erythrocytes
Endothelial
Cartilage
Pharyneal arch
Olfactory bulb
Muscle
Retina neurogenesis
Cranial ganglion
Dorsal diencephalon
Neuron
Pigment cell (iridophore)
Retina (photoreceptor precursor cells)
Hindbrain
Neural crest
Ventral diencephalon
Pigment cell (neural crest derived)
retina (amacrine)
Progenitors
Ventral midbrain
Floor plate
Otic vesicle
Periderm
Epidermis
Neutrophils
UMAP2
UMAP1
C
Ratio of Cells
1.00
0.75
0.50
0.25
0.00
ctrl_1d
ko_1d
ctrl_2d
ko_2d
Conditions
Cell Type
Neuron
Pharyneal arch
Progenitors
Retina neurogenesis
Erythrocytes
Ventral diencephalon
Cartilage
Ventral midbrain
Dorsal diencephalon
Retina (photoreceptor precursor cells)
Muscle
Epidermis
Olfactory bulb
Cranial ganglion
Otic vesicle
Hindbrain
Endothelial
retina (amacrine)
Periderm
Neural crest
Neutrophils
Pigment cell (iridophore)
Pigment cell (neural crest derived)
Floor plate
D
Progenitors ctrl_2d vs ko_2d enrich GO terms
chromatin silencing
negative regulation of transcription, DNA−templated
nucleosome positioning
nucleosome assembly
negative regulation of DNA metabolic process
regulation of DNA recombination
chromatin organization
DNA packaging
microtubule depolymerization
negative regulation of cellular component organization
regulation of microtubule polymerization or depolymerization
defense response to Gram−positive bacterium
microtubule polymerization or depolymerization
chaperone cofactor−dependent protein refolding
neurotransmitter secretion
regulation of microtubule cytoskeleton organization
cellular protein complex disassembly
neurotransmitter transport
response to heat
microtubule cytoskeleton organization
0
5
10
15
20
25
−log10(p.adjust)
E
stmn1a
stmn1b
stmn2a
stmn2b
stmn3
stmn4
stmn4l
ctrl_1d
ko_1d
ctrl_2d
ko_2d
Progenitors.ctrl_1d
Progenitors.ko_1d
Progenitors.ctrl_2d
Progenitors.ko_2d
F
betaPix^ct/ct glia
betaPix^m/m glia
Relative expression
1.5
1.0
0.5
0.0
****
***
betaPix
stmn1a
stmn1b
stmn4l
ppfia3
G
betaPix^ct/ct glia
gfap:GFP-Cre; betaPix^ct/ct glia
H
stmn1a
stmn1b
stmn4l
48 hpf
betaPix^ct/ct
gfap:GFP-Cre; betaPix^ct/ct
24/24
24/24
24/24
20/20
19/20
25/29
Scale bar: 500 µm

Figure 5

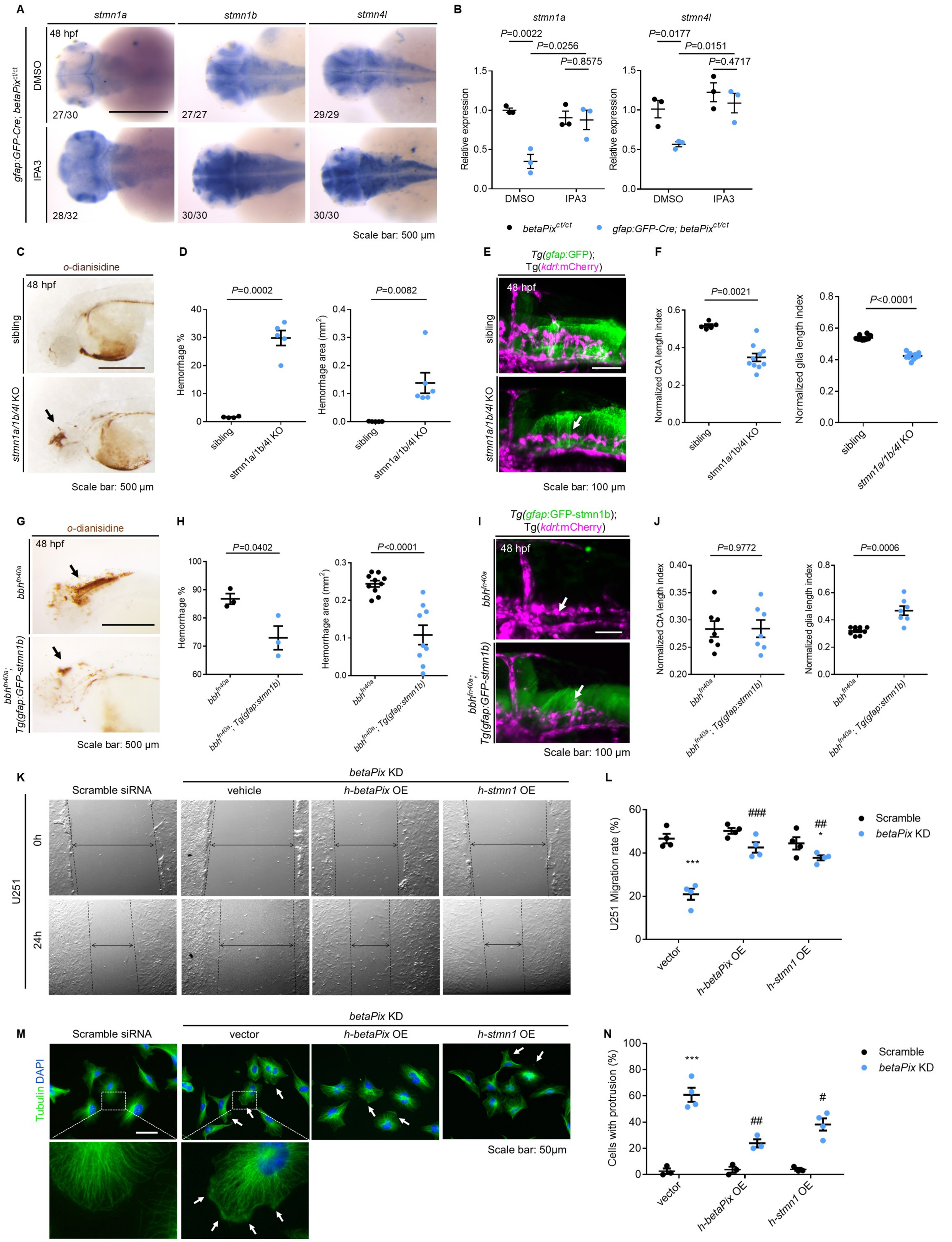
A
stmn1a
stmn1b
stmn4l
48 hpf
gfap:GFP-Cre; betaPix ct/ct
DMSO
IPA3
27/30
27/27
29/29
28/32
30/30
30/30
Scale bar: 500 μm
B
stmn1a
stmn4l
P=0.0022
P=0.0256
P=0.8575
P=0.0177
P=0.0151
P=0.4717
Relative expression
DMSO
IPA3
betaPix ct/ct
gfap:GFP-Cre; betaPix ct/ct
C
o-dianisidine
48 hpf
sibling
stmn1a/1b/4l KO
Scale bar: 500 μm
D
P=0.0002
P=0.0082
Hemorrhage %
Hemorrhage area (mm2)
sibling
stmn1a/1b/4l KO
E
Tg(gfap:GFP);
Tg(kdrl:mCherry)
48 hpf
Scale bar: 100 μm
F
P=0.0021
P<0.0001
Normalized CtA length index
Normalized glia length index
G
o-dianisidine
48 hpf
bbh fn40a
bbh fn40a; Tg(gfap:GFP-stmn1b)
Scale bar: 500 μm
H
P=0.0402
P<0.0001
Hemorrhage %
Hemorrhage area (mm2)
bbh fn40a
bbh fn40a; Tg(gfap:stmn1b)
I
Tg(gfap:GFP-stmn1b);
Tg(kdrl:mCherry)
48 hpf
Scale bar: 100 μm
J
P=0.9772
P=0.0006
Normalized CtA length index
Normalized glia length index
K
betaPix KD
Scramble siRNA
vehicle
h-betaPix OE
h-stmn1 OE
U251
0h
24h
L
U251 Migration rate (%)
Scramble
betaPix KD
vector
h-betaPix OE
h-stmn1 OE
M
betaPix KD
Scramble siRNA
vector
h-betaPix OE
h-stmn1 OE
Tubulin DAPI
Scale bar: 50μm
N
Cells with protrusion (%)
Scramble
betaPix KD
vector
h-betaPix OE
h-stmn1 OE

Figure 6

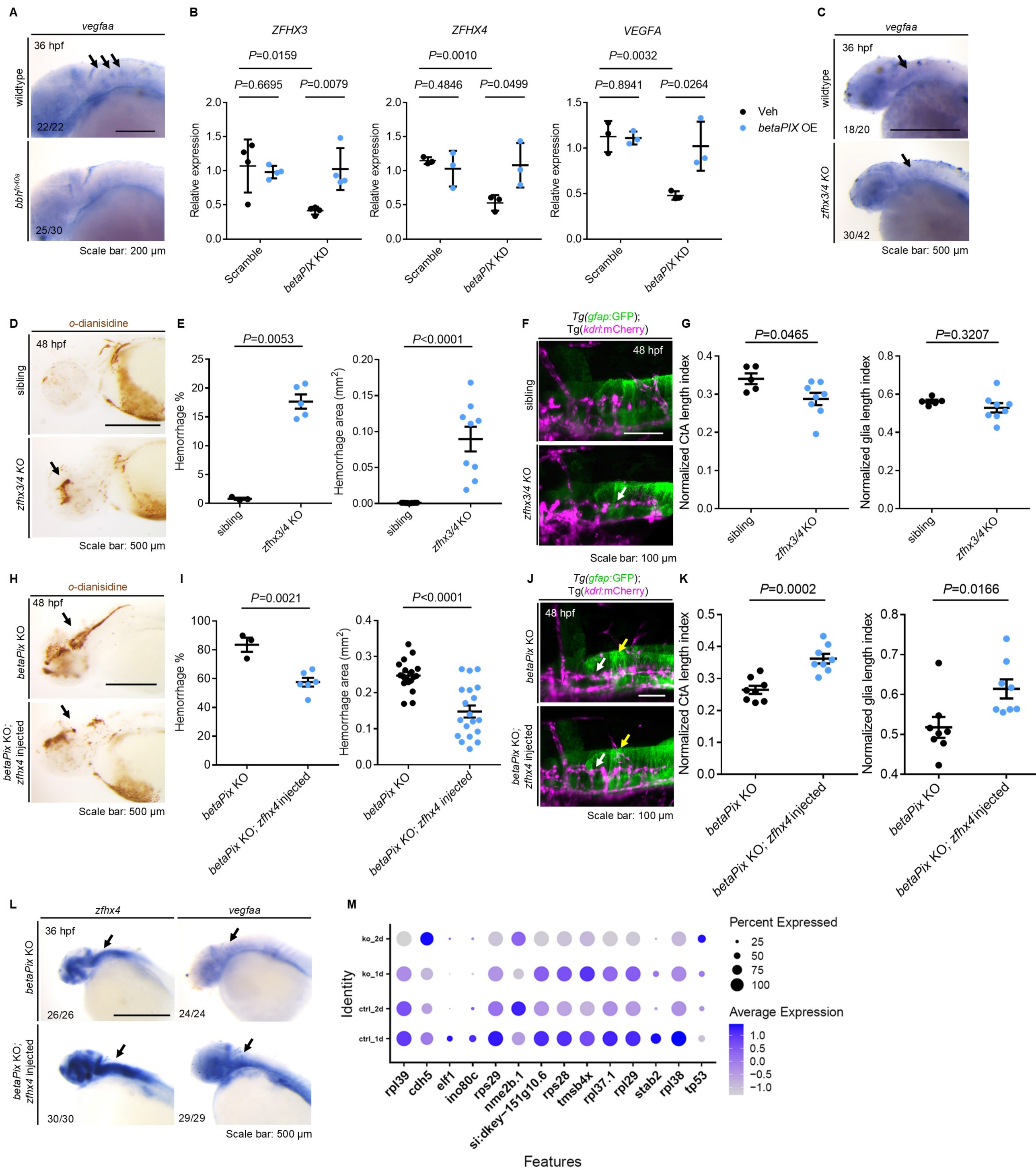
A
vegfaa
36 hpf
wildtype
22/22
bbh^fn40a
25/30
Scale bar: 200 µm
B
ZFHX3
P=0.0159
P=0.6695
P=0.0079
ZFHX4
P=0.0010
P=0.4846
P=0.0499
VEGFA
P=0.0032
P=0.8941
P=0.0264
Relative expression
Scramble
betaPIX KD
Veh
betaPIX OE
C
vegfaa
36 hpf
wildtype
18/20
zfhx3/4 KO
30/42
Scale bar: 500 µm
D
o-dianisidine
48 hpf
sibling
zfhx3/4 KO
Scale bar: 500 µm
E
P=0.0053
Hemorrhage %
P<0.0001
Hemorrhage area (mm²)
sibling
zfhx3/4 KO
F
Tg(gfap:GFP);
Tg(kdrl:mCherry)
48 hpf
sibling
zfhx3/4 KO
Scale bar: 100 µm
G
P=0.0465
Normalized CtA length index
P=0.3207
Normalized glia length index
sibling
zfhx3/4 KO
H
o-dianisidine
48 hpf
betaPix KO
betaPix KO; zfhx4 injected
Scale bar: 500 µm
I
P=0.0021
Hemorrhage %
P<0.0001
Hemorrhage area (mm²)
betaPix KO
betaPix KO; zfhx4 injected
J
Tg(gfap:GFP);
Tg(kdrl:mCherry)
48 hpf
betaPix KO
betaPix KO; zfhx4 injected
Scale bar: 100 µm
K
P=0.0002
Normalized CtA length index
P=0.0166
Normalized glia length index
betaPix KO
betaPix KO; zfhx4 injected
L
zfhx4
vegfaa
36 hpf
betaPix KO
26/26
24/24
betaPix KO; zfhx4 injected
30/30
29/29
Scale bar: 500 µm
M
Identity
ko_2d
ko_1d
ctrl_2d
ctrl_1d
rpl39
cdh5
elf1
ino80c
rps29
nme2b.1
si:dkey-151g10.6
rps28
tmsb4x
rpl37.1
rpl29
stab2
rpl38
tp53
Features
Percent Expressed
25
50
75
100
Average Expression
1.0
0.5
0.0
−0.5
−1.0

Figure 7

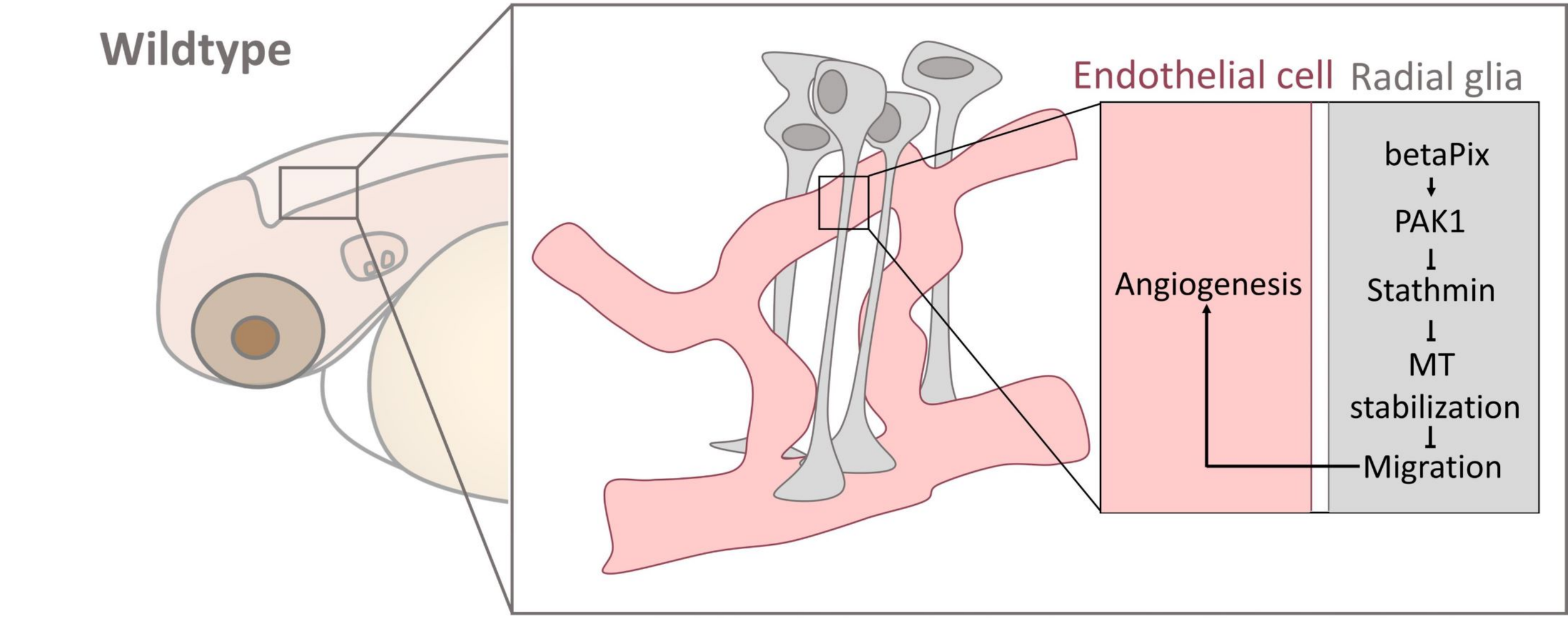
Wildtype
Endothelial cell
Radial glia
betaPix
PAK1
Stathmin
MT
stabilization
Migration
Angiogenesis

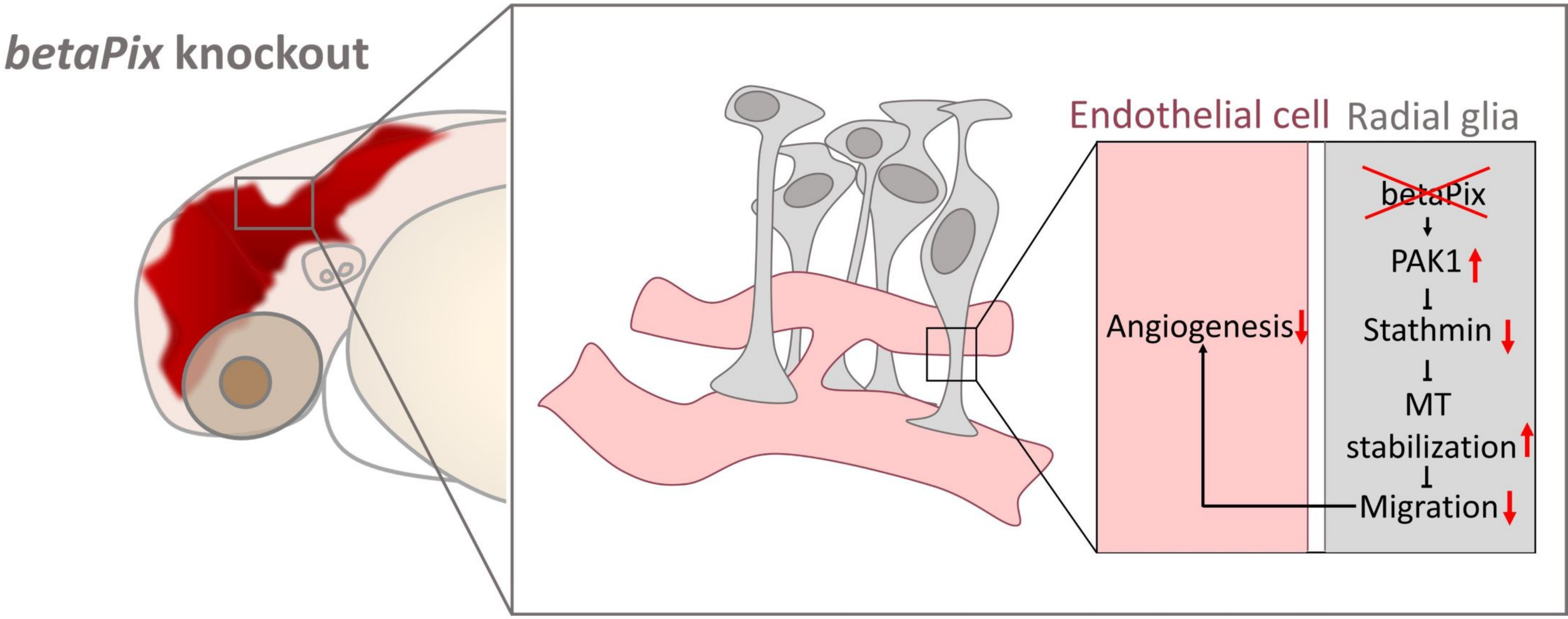
betaPix knockout
Endothelial cell
Radial glia
betaPix
PAK1
Stathmin
MT
stabilization
Migration
Angiogenesis